The Parkinson's drug entacapone disrupts gut microbiome homeostasis via iron sequestration

Fátima C. Pereira[a,b,+,*], Xiaowei Ge[c,+], Jannie Munk Kristensen[a], Rasmus H. Kirkegaard[a,e], Klara Maritsch[a], Yifan Zhu[d], Marie Decorte[a], Bela Hausmann[e,f], David Berry[a], Kenneth Wasmund[a,§], Arno Schintlmeister[a], Thomas Boettcher[a,g], Ji-Xin Cheng[c,h*], Michael Wagner[a,i*]

[a]Centre for Microbiology and Environmental Systems Science, Department of Microbiology and Ecosystem Science, University of Vienna, Vienna, Austria.
[b]School of Biological Sciences, University of Southampton, Southampton, United Kingdom.
[c]Department of Electrical & Computer Engineering, Boston University, Boston, Massachusetts, USA.
[d]Department of Chemistry, Boston University, Boston, Massachusetts, USA.
[e]Joint Microbiome Facility of the Medical University of Vienna and the University of Vienna, Vienna, Austria.
[f]Department of Laboratory Medicine, Medical University of Vienna, Vienna, Austria.
[g]Faculty of Chemistry, Department of Biological Chemistry, University of Vienna, Vienna, Austria.
[h]Photonics Center, Boston University, Boston, Massachusetts, USA.
[i]Department of Chemistry and Bioscience, Aalborg University, Aalborg, Denmark.

[+] These authors contributed equally
[§] Present address: School of Biological Sciences, University of Portsmouth, Portsmouth, United Kingdom.

***Corresponding authors**: f.c.pereira@soton.ac.uk, michael.wagner@univie.ac.at, jxcheng@bu.edu

Abstract

Increasing evidence shows that many human-targeted drugs alter the gut microbiome, leading to implications for host health. However, much less is known about the mechanisms by which drugs target the microbiome and how drugs affect microbial function. Here we combined quantitative microbiome profiling, long-read metagenomics, stable isotope probing and single-cell chemical imaging to investigate the impact of two widely prescribed nervous system-targeted drugs on the gut microbiome. *Ex vivo* supplementation of physiologically relevant concentrations of entacapone or loxapine succinate to faecal samples significantly impacted the abundance of up to one third of the microbial species present. Importantly, we demonstrate that the impact of these drugs on microbial metabolism is much more pronounced than their impact on abundances, with low concentrations of drugs reducing the activity, but not the abundance of key microbiome members like *Bacteroides, Ruminococcus* or *Clostridium* species. We further demonstrate that entacapone impacts the microbiome due to its ability to complex and deplete available iron, and that microbial growth can be rescued by replenishing levels of microbiota-accessible iron. Remarkably, entacapone-induced iron starvation selected for iron-scavenging organisms carrying antimicrobial resistance and virulence genes. Collectively, our study unveils the impact of two under-investigated drugs on whole microbiomes and identifies metal sequestration as a mechanism of drug-induced microbiome disturbance.

Main

Drugs initially designed to specifically target human cells often can affect microbes as well[1]. As a result of poor gastrointestinal absorption and/or biliary secretion, many of these drugs reach the large intestine where they encounter - and potentially interact with - hundreds to thousands of different microbial species that play important roles in various aspects of human physiology[1,2,3]. Indeed, several cohort studies have reported significant associations between the use of medication and shifts in gut microbial composition and function[4,5,6,7]. While the cross-sectional nature of these large cohort studies hinders the establishment of causality, *in vitro* studies have been pivotal for systematically evaluating direct effects of human-targeted drugs on gut microbes. A landmark study assessing the antimicrobial effect of 835 human-targeted drugs against a panel of 40 cultured gut microbes revealed that a significant proportion (24%) of drugs could inhibit the growth of at least one gut bacterial strain *in vitro*[1]. An additional study testing the effect of a smaller panel of drugs on faecal samples by metaproteomics demonstrated selective anti- and/or pro-microbial activity for the great

83 majority of drugs tested, with a significant fraction of drugs also shifting microbiome
84 composition[8]. Of note, this study demonstrated that bacterial function could shift in response
85 to drugs without a change in taxon abundance, thus highlighting the need for using metrics
86 other than abundance when investigating the impact of drugs. Importantly, the interaction
87 between the microbiome and drugs is bidirectional, with many studies clearly demonstrating
88 that gut microbes can also actively metabolize[9,10,11,12], and under certain circumstances
89 bioaccumulate[13], pharmaceutical drugs. While several studies to date have shed light on the
90 nature and extent of microbe-driven drug transformations[9,10,11], mechanistic details for human-
91 targeted drug impact on the microbiome remain to be elucidated.

92 One hypothesis is that drugs can change intestinal microenvironments such as pH or
93 osmolarity, and by doing so, directly affect bacterial growth[14]. Another explanation is that
94 drugs interact with structural analogues of their human targets within bacteria, thus interfering
95 with cellular processes also in microbes[15]. Drug-microbiome interactions have been shown to
96 modulate the therapeutic effect of the drug, contribute to its side effects, or both[11,16,17,18].
97 Importantly, in certain cases, drug-induced microbiome changes might also contribute to other
98 diseases. For instance, proton pump inhibitors (PPIs) cause major shifts in the gut
99 microbiome[19], leading to decreased resistance to colonisation by enteric pathogens such as
100 *Clostridioides difficile*, *Campylobacter* and *Salmonella*[20]. Furthermore, PPIs-induced shifts in
101 the microbiome during early childhood have been linked to obesity[21].

102 Among the human-targeted drugs tested *in vitro*, compounds that target the nervous system
103 seem to exhibit stronger anti-commensal activity against gut bacteria compared to other
104 tested drug classes[1]. Indeed, several studies have reported a strong and selective inhibitory
105 activity of antipsychotics and antidepressants on gut microbial strains and microbiomes[22,23,24].
106 This is concerning, given the growing number of studies implicating the microbiome in many
107 neuropsychiatric disorders[25], and the widespread and rising use of this class of
108 pharmaceuticals worldwide[26]. Thus, a better mechanistic understanding of drug-microbiome
109 interactions in the context of nervous system-targeted medications may facilitate novel ways
110 to improve efficacy and/or minimize side effects of therapies for such disorders.

111 Here, we investigate the effects of two nervous system-targeted drugs on whole gut
112 microbiomes using a suite of complementary functional microbiome approaches. These aimed
113 at investigating the effects of the drugs in the context of whole microbial communities, which
114 more closely resembles their effects *in situ*, and to therefore examine most key members of
115 the gut microbiome. We studied two commonly used drugs: i) entacapone, a catechol-O-
116 methyltransferase (COMT) inhibitor that acts by preventing the degradation of levodopa, the
117 main drug used in the treatment of Parkinson's disease[27]; ii) loxapine succinate, a tricyclic
118 antipsychotic medication primarily used in the treatment of schizophrenia[28]. These drugs,

119 whose yearly total prescription exceeds 30 million tablets only in the US[29], belong to different
120 therapeutic classes and were shown to be selective in their anti-commensal activity against a
121 panel of 40 cultured gut strains, with entacapone predominantly targeting Gram-positive
122 organisms of the Firmicutes phylum and loxapine succinate only taxa within the Gram-
123 negative order Bacteroidales[1]. We demonstrate that the impact of either drug on microbiome
124 composition and/or activity extends beyond the taxa initially detected *in vitro* in pure culture,
125 with entacapone causing strong shifts in microbiome composition. This prompted us to look
126 for the cause of these shifts. We identified microbial iron deprivation, driven by the ability of
127 entacapone to complex iron, as the main mechanism behind entacapone's strong modulatory
128 effect. These results advance our understanding of the impact of nervous-system targeted
129 drugs on whole microbial communities and reveal micronutrient-deprivation as a mechanism
130 through which entacapone disrupts the microbiome.
131

132 # Results

133 **Nervous-system targeted drugs affect microbiome composition and abundance**

134 To evaluate the impact of entacapone (ENT) and loxapine succinate (LOX) on whole gut
135 microbiome communities, we incubated freshly collected faecal samples from healthy adult
136 individuals in sM9 medium with two different concentrations of each drug dissolved in
137 dimethylsulfoxide (DMSO) (Fig.1a, see Methods). The low drug concentration (ENT-Low,
138 LOX-Low, 20 μM) was previously used in a screening aimed at determining drug effects on
139 pure culture isolates, while the high concentrations (ENT-Hi, 1965 μM, LOX-Hi, 100 μM) were
140 based on estimated colon concentrations for each drug, and were included to better reflect
141 the exposure of gut microbes to these drugs in the large intestine[1] (see Methods). After short
142 incubation times (6 and 24 hours) under anaerobic conditions at 37 °C, samples were
143 collected and processed to determine: i) changes of the total microbial loads; ii) microbial
144 community profile dynamics based on 16S rRNA gene amplicon sequencing; iii) reconstructed
145 microbial genomes based on long-read metagenomics and iv) single-cell microbial activity
146 changes via tracing of the incorporation of deuterium from isotopically-labelled heavy water
147 (D_2O) into single cells of microbiota by chemical imaging based on stimulated Raman
148 scattering spectroscopy (SRS)[30] (Fig.1a).

149 Counts of total microbial cell loads by flow cytometry in samples incubated with or without
150 drugs revealed that supplementation of a physiologically relevant concentration of
151 entacapone (ENT-Hi) significantly reduced the numbers of microbial cells over time, when
152 compared to all other tested conditions (Fig.1b, Supplementary Table 1). Major shifts in the
153 microbial community composition, as determined by 16S rRNA gene amplicon sequencing

analyses, were detected in response to ENT-Hi, LOX-Hi and LOX-Low treatments (Fig.1c), and in the case of ENT-Hi these were also accompanied by shifts in alpha diversity (Extended Data Fig.1a,b; Supplementary Table 2,3).

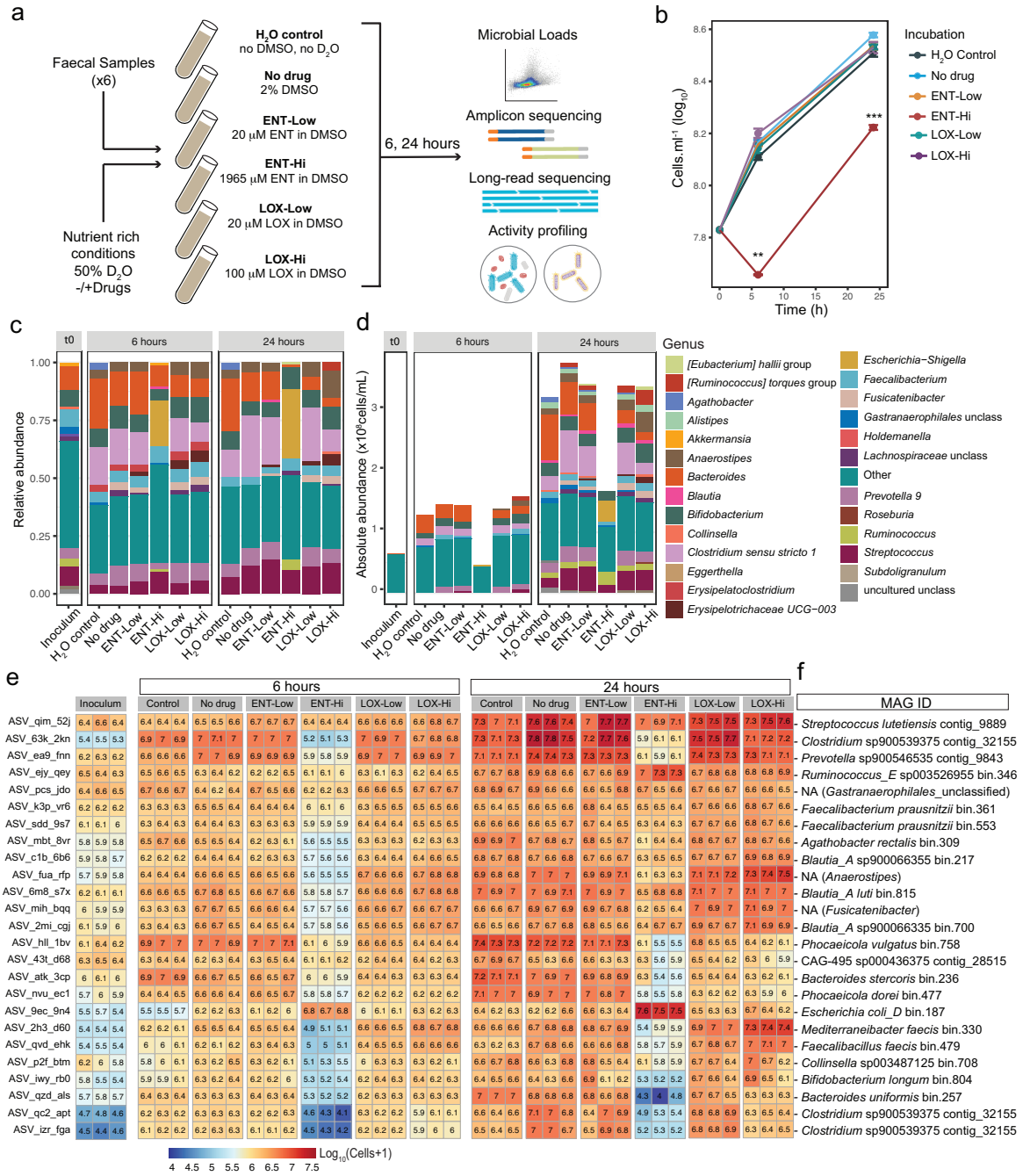

Figure 1. Drug-supplementation of faecal samples impacts biomass accumulation and microbiota composition. a. Schematic representation of faecal sample incubations with the drugs entacapone (ENT) and loxapine (LOX). As indicated, two different concentrations of each drug were used (Low and Hi). Incubations were performed in the presence of 50% heavy water (D_2O) and 2% DMSO in the medium (either sM9 or BHI), except for the H_2O control that consisted of medium without D_2O or DMSO. After 6 or 24 hours of incubation, samples were collected for further analyses (see Methods). All incubations were performed in triplicates. **b.** Total microbial cell loads in faecal sample incubations described in (A), at the start of the incubation (time=0 hours) and after 6 and 24 hours, respectively. Total cell loads were assessed by flow cytometry. **p<0.01; ***p<0.001; unpaired two-sample t-test with "No drug" used as the reference. **c, d.** Relative (**c**) and absolute (**d**) genus abundance profiles of faecal microbial communities incubated for 6 or 24 hours as described in (**a**) and assessed by 16S rRNA gene amplicon sequencing. The community

169 composition at 0 hours (inoculum) is also shown. All genera present at a relative abundance below 0.025 or
170 absolute abundance below $6x10^6$ cells.ml^{-1} were assigned to the category "Other". "unclass": unclassified.
171 **e**. Heatmap showing the absolute abundance, expressed in log_{10}(cells+1), of the 25 most abundant ASVs
172 detected across all samples. Each column displays data from one replicate. **f**. Metagenome-assembled
173 genomes (MAGs) with 16S rRNA gene sequences matching ASVs shown in (**e**). MAGs were retrieved by
174 metagenomic sequencing of the initial faecal samples using Oxford Nanopore sequencing (see Methods
175 and Supplementary Table 7). 'NA" indicates no match of the ASV sequence to each MAG 16S rRNA gene
176 sequence.

177

178 By integrating total microbial counts with 16S rRNA gene amplicon sequencing data[31], we
179 determined absolute abundances for all detected taxa (Fig.1d). Importantly, absolute
180 abundance data confirmed that the employed incubation conditions enabled an increase in
181 abundance for nearly all the taxa initially present in faecal samples (Fig.1e: No drug versus
182 inoculum; Supplementary Table 4) and thus allowed tracking drug-induced activity and
183 abundance changes of microbiome members. Absolute abundances of genera such as
184 *Bacteroides* or *Clostridium sensu stricto* 1 decreased in both ENT-Hi and LOX-Hi samples
185 compared to the DMSO control (Fig.1d). However, many of the detected effects were drug-
186 specific, with ENT-Hi decreasing and LOX-Hi increasing total abundances of the genera
187 *Anaerostipes, Fusicatenibacter*, *Ruminococcus torques* group, *Eubacterium hallii* group,
188 *Erysipelotrichaceae* group UG-003 and *Roseburia*. Abundances of several genera were
189 significantly altered in response to ENT-Hi only: *Escherichia-Shigella and Ruminococcus*
190 increased in abundance, and genera such as *Alistipes*, *Streptococcus* or *Blautia* decreased
191 (Fig.1d,e; Supplementary Table 5). A similar impact of ENT-Hi on microbial biomass
192 accumulation and on the overall community composition could also be observed when we
193 used a different, nutrient rich medium (BHI) for the incubations (Extended Data Fig.1c-g).

194 Differential abundance analysis indicated that the abundance of 29.4% of all 16S rRNA gene
195 amplicon sequencing variants (ASVs) were significantly impacted by ENT-Hi after 24 hours
196 of incubation, 11.8% of ASVs were impacted by LOX-Hi, and only 3.6% and 6.0% of ASVs
197 were impacted by ENT-Low and LOX-Low, respectively (see Methods, Supplementary Table
198 5). Interestingly, LOX-Low resulted in growth inhibition patterns that differ from the ones
199 observed when the same drug was supplemented to gut members grown under isolation[1],
200 where it only specifically inhibits growth of Bacteroidales strains. Our results show that other
201 Gram-negatives and several Gram-positive species are affected by LOX-Low in the context
202 of whole microbiome communities (Supplementary Table 5). These include
203 *Erysipelotrichaceae* spp., *Oscillospiraceae* spp. and *Lachnospiraceae* spp., suggesting a
204 cross-sensitization to loxapine in the context of the community. For ENT-Low, only a very low
205 number of organisms were significantly impacted and were mostly Firmicutes, which agrees
206 with previous reports[1] (Supplementary Table 5).

207 Using long-read metagenomic sequencing of the starting faecal sample material, we retrieved
208 a total of 1049 metagenome-assembled genomes (MAGs), 11 of which are complete
209 genomes and 255 are medium- or high-quality genomes (Supplementary Tables 6 and 7).
210 BLASTn[32] analysis enabled us to link 16S rRNA gene sequences of ASVs to MAGs that
211 contained 16S rRNA genes and to follow drug-driven community shifts at a higher taxonomic
212 resolution (Fig.1e,f). This revealed that ASVs classified as *Escherichia* and *Ruminococcus*
213 taxa thriving in ENT-Hi give exact hits to the 16S rRNA genes in genomes of *E. coli* and *R.*
214 *bromii*. These analyses also indicated that LOX-Hi conditions selectively promoted the growth
215 of taxa like *Mediterraneibacter faecis*, *Faecalibacillus faecis* and *Blautia_A*. Species such as
216 *Clostridium* sp900539375 (*Clostridium sensu stricto* 1 based on SILVA taxonomy) and several
217 *Bacteroides* species *(B. uniformis, B. stercoris, Phocaeicola dorei* - formerly *B. dorei,* and *P.*
218 *vulgatus* - formely *B. vulgatus*) were totally or partially inhibited by the presence of high
219 concentrations of either drug, but the effect of ENT-Hi is much more pronounced than that of
220 LOX-Hi (Fig.1e,f). On the other hand, *Prevotella* sp900546535 and several Gram-positive
221 organisms such as *Streptococcus lutetiensis*, *Collinsella* sp003487125, *Bifidobacterium*
222 *longum*, *Mediterraneibacter faecis* or *Faecalibacillus faecis* showed growth inhibition by ENT-
223 Hi only (Fig.1e,f). All together these results reveal a strong but distinct impact of entacapone
224 and loxapine at physiological concentrations on microbiota composition and abundance, with
225 entacapone having a much more pronounced effect than loxapine.
226

227 **Nervous system-targeted drugs can alter microbial metabolism without impacting**
228 **microbial abundance**

229 Next, we evaluated the effect of these drugs on microbial activity at the single-cell level and
230 explored whether drug exposure that did not cause major shifts in microbiome abundance
231 within 24 hours of incubation did, nevertheless, impact their activity. To determine drug-
232 induced changes in microbial activity, we added D_2O as universal metabolic tracer[33,34,35] to
233 our incubations (Fig.1a). In complex microbial communities, all metabolically active cells will
234 incorporate deuterium (D) from D_2O into their biomass during synthesis of new
235 macromolecules[34]. The newly formed carbon-deuterium (C-D) bonds can then be used as a
236 read-out of microbial activity. Detection and quantification of C-D levels in single microbial
237 cells can be achieved using SRS, a method that efficiently excites the Raman active
238 vibrational modes coherently with two synchronized ultrafast lasers[36,37,38]. We have
239 successfully combined SRS with fluorescence *in situ* hybridization (FISH) in the past to
240 determine gut microbiome response to sugars with high-throughput[30]. Using an optimized
241 SRS-FISH platform that provides even higher throughput and sensitivity than the previous
242 setup (Supplementary Information text, Extended Data Fig.2), we measured around thirty

243 thousand individual microbiota cells after 6 and 24 hours of incubation in the presence of the
244 drugs and in controls (Fig.2a,b). An unexpected, non-vibrational signal was detected in
245 samples that were incubated with ENT-Hi and thus these samples were excluded from SRS-
246 based activity measurements and the origin of this signal was further explored as detailed in
247 the next section. As expected, in the absence of the drugs, nearly all of the analyzed cells
248 were detected as active in the incubation medium, with 90% and 98% of cells displaying
249 $\%CD_{SRS}$ values above threshold at 6 hours and 24 hours of incubation, respectively (Fig.2b,
250 Supplementary Table 8). Addition of either ENT-Low, LOX-Low or LOX-Hi resulted in a
251 significantly reduced fraction of total active cells, as well as in a significant reduction of single-
252 cell metabolic activity. This reduction was more pronounced for LOX-Hi, followed by LOX-Low
253 and ENT-Low (Fig.2b). Thus, these drugs clearly impacted microbial activity within
254 communities, even after short incubation times and under conditions where no impacts on
255 their overall abundances were detected (Fig.1b).

256 To examine the activity of specific populations of the microbiome within the complex
257 communities, we targeted six distinct abundant taxa of interest using SRS-FISH, which
258 enabled us to determine the activity of individual cells from these taxa. Both published as well
259 as newly designed and optimized oligonucleotide probes targeting 16S and 23S rRNA
260 sequences predicted from MAGs retrieved by metagenomics were used for this purpose
261 (Supplementary Table 9). Targeted taxa included organisms whose abundances were both
262 negatively and positively impacted by drugs. We then evaluated the levels of activity of the
263 targeted populations using picosecond SRS (Fig.2c, Extended Data Fig.2). Both LOX-Low
264 and LOX-Hi incubations significantly reduced the activity of all targeted gut microbiota
265 members except for *E. coli* (Fig.2d). Interestingly, *Clostridium* sp900539375, *B. uniformis*,
266 *Ruminococcus bromii* and *P. dorei* show reduced activity in LOX treatments, but only the
267 abundance of *P. dorei* and *Clostridium* sp900539375 was negatively impacted (Fig.2d,e;
268 Supplementary Table 10). LOX-Low and LOX-Hi seem to strongly inhibit *P. dorei* growth
269 within 6 hours (Fig. 1e), probably rendering most cells of this taxon undetectable by FISH, as
270 the low ribosome content of non-active cells hinders FISH detection. We speculate that only
271 a few drug-resistant *P. dorei* cells remained active enough to be detected by FISH, and these
272 cells were not strongly impacted in activity (Fig.2c,d). A comparable decrease in activity was
273 detected for *Streptococcus* spp., but in this case this decrease was surprisingly accompanied
274 by a slight increase in abundance at 6 hours (Fig.2d,e). However, from 6 to 24 hours, we
275 detect a decrease of the population represented by *Streptococcus lutentiensis* MAG in the
276 presence of LOX compared to the control (Fig. 1e,f), which could be an effect of the lower
277 activities detected by SRS in the LOX conditions at 6 hours. In summary, SRS-FISH provided
278 new insights into the impact of ENT and LOX on the activities of specific microbiome

members, which are often masked when only considering abundance data from relatively short incubation experiments.

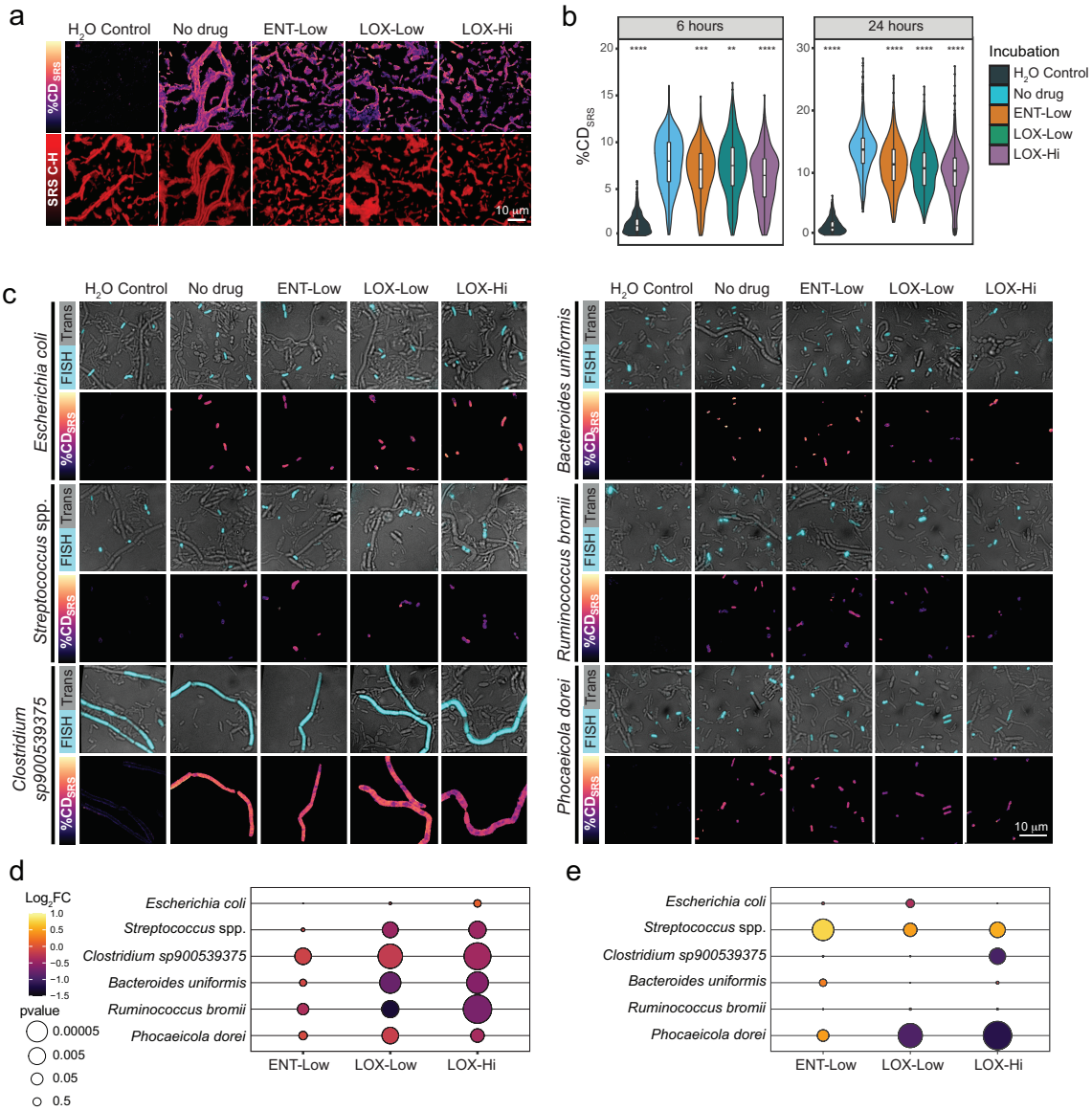

Figure 2. Metabolic activity of drug-incubated single-microbiome cells measured by deuterium incorporation via SRS. a. Representative SRS images of faecal samples incubated with the indicated drugs for 6 hours. The measure $\%CD_{SRS}$ indicates different levels of microbial activity. $\%CD_{SRS}$ distribution images are displayed on top and C-H for biomass visualization (log scaled) on the bottom. $\%CD_{SRS}$ scaling: minimum 0, maximum 20%. **b.** Single-cell $\%CD_{SRS}$ values in each analyzed sample. Violin plots illustrating summary statistics (median, first and third quartiles, with the extended lines representing the minimum and maximum values within 1.5 interquartile ranges from the first and third quartiles). **p=0.0043, ***p=5.2e-12, **** p<2e-16, Wilcoxon test using "No drug" as the reference. **c.** Drug-incubated faecal samples were hybridized with fluorescently-labeled oligonucleotide probes targeting *E. coli* (Ecol_268), *Streptococcus* and *Lactococcus* species (Strc_493), *Clostridium* sp900539375 (*Clostridium sensu stricto 1,* Clo_648), *Ruminococcus bromii* (Brom_2036), *B. uniformis* (Buni_1001), and *Phocaeicola dorei* (Bado_374) (all shown in cyan, Supplementary Table 9). For each targeted group, top rows show representative images obtained by overlay of transmitted light (grey) and fluorescence intensity (cyan). Bottom rows show the corresponding SRS images (displaying $\%CD_{SRS}$) for the FISH-targeted microbes ($\%CD_{SRS}$ values of other microbes are not displayed for the sake of visibility). $\%CD_{SRS}$ scaling: minimum 0, maximum 20%. Scale bar, 10 µm. **d.** Bubble plot denoting the fold change (FC, represented as Log_2FC) in activity levels (calculated as $\%CD_{SRS}$) for the taxa targeted by FISH and incubated with drugs relative to "No drug" incubations. **e.** Bubble plot denoting the FC in absolute abundances for the taxa targeted by FISH and incubated with drugs relative to "No drug" incubations, as determined by DeSeq2.

Entacapone bioaccumulates in microbiota cells

Gut microbes have been shown to bioaccumulate some drugs leading to depletion of the drug from the surrounding environment[13,39]. As ENT-Hi samples showed a strong, Raman unspecific signal during SRS pump-probe detection, we explored the origin of this signal and concluded that this is a photothermal (PT) signal originating from entacapone bioaccumulation within microbial cells (Supporting Information Text). By mapping the intensity of this PT signal from ENT-Hi samples and controls (Fig.3a), we were able to show that the signal from entacapone occurred in a large fraction of microbial cells that had been incubated with the drug and washed before being fixed for analysis, but only in very few cells that had been fixed prior to incubation with the drug (i.e., dead cells) (Fig.3b,c, Supplementary Table 11).

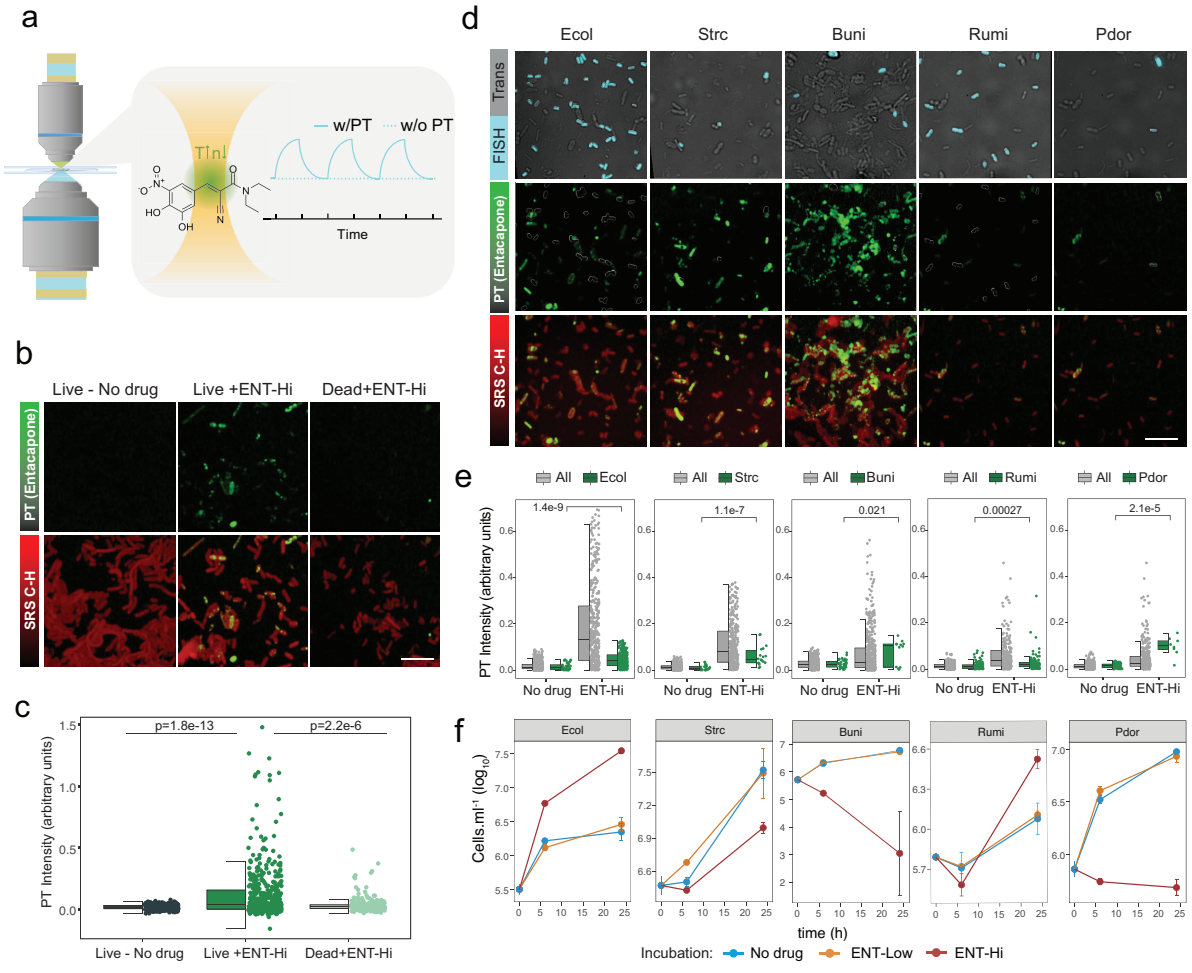

Figure 3. Photothermal imaging of entacapone bioaccumulation by microbiota cells. a. Schematic illustration of the time-dependent signal obtained from a solution of 10 mM entacapone in DMSO, with photothermal (w/PT) and without photothermal (w/o PT) detection. **b.** Photothermal signal intensity distribution from entacapone, shown in green (PT, determined by photothermal imaging), and C-H signal, shown in red, of live and dead (PFA fixed) microbiota cells incubated in the presence (+) or absence (-) of ENT-Hi for 6 hours. PT channel contrast: min 0 max 1.8. C-H signals are represented on a log scale. Scale bar, 10 µm. **c.** Single-cell photothermal signal intensity distribution in samples shown in (a). p-values were determined using an unpaired two-sample Wilcoxon test. **d.** Representative images of faecal samples incubated with entacapone for 6 hours followed by hybridization with fluorescently-labeled oligonucleotide probes targeting *E. coli* (Ecol), *Streptococcus* and *Lactococcus* (Strc), *Ruminococcus bromii* (Rumi), *B. uniformis* (Buni), and *Phocaeicola dorei* (Pdor) (see Supplementary Table 9). FISH-probe signals from

hybridized cells (in cyan) were detected using widefield fluorescence microscopy (top panel). Photothermal signal maps from entacapone (PT, in green) are shown in the middle (cells targeted by FISH are shown with respective white contour lines). Entacapone PT signals overlayed with SRS C-H signals (in red) are shown in the bottom panel. PT channel contrast: min 0 max 1.8. C-H signals are represented on a log scale. Scale bar, 8 µm. **e.** Single-cell photothermal signal distribution in samples shown in (c). p-values were determined using the unpaired two-sample Wilcoxon test. **f.** Time series of the absolute abundance of the respective taxa targeted by FISH in No drug, Ent-Low and ENT-Hi incubations. In **c**, **e** boxes represent the median, first and third quartile. Whiskers extend to the highest and lowest values that are within one and a half times the interquartile range.

To identify the main drug accumulating taxa, we further looked at the entacapone distribution among populations targeted with the FISH probes described above (Fig.3d, Supplementary Table 9). All of the targeted populations displayed entacapone signals to different intensities. While *P. dorei* and, to a lesser extent *Streptococcus* spp. and *E. coli,* seemed to be strong entacapone accumulators, only a small percentage of *R. bromii* and part of the *B. uniformis* population accumulated entacapone (Fig.3d,e). High entacapone signals were also detected in cells not targeted by FISH (Fig.3e). We further confirmed the ability of *P. dorei* to accumulate entacapone when grown in pure culture (Extended Data Fig.5). Interestingly, while entacapone accumulation drastically inhibited the growth of *P. dorei* as a microbiome community member and in pure culture, it did not affect *Streptococcus* growth in the community to the same extent and showed even growth promotion for *E. coli* (Fig.3e). Thus, bioaccumulation of the drug led to growth inhibition for certain taxa, whereas others were unaffected or even stimulated in growth. This is in line with findings reported for the well-studied antidepressant duloxetine, which was also found to be bioaccumulated by gut microbiota taxa without impacting their growth[13].

Entacapone chelates iron and induces iron starvation in whole microbiome populations

Entacapone's nitrocatechol group can act as a bidentate ligand, chelating and forming stable complexes with transition metal ions such as iron (Fe) through the catecholate oxygen atoms[40]. Using an assay widely applied to detect siderophores and other strong Fe-chelating agents in solution, we confirmed entacapone's ability to chelate ferric iron (Fe(III)) (Fig.4a). Binding of entacapone to metal ions such as Fe(III) has been proposed to occur via formation of a tris complex[40]. The stability constant of entacapone's association with Fe (pFe(III)=19.3) has been demonstrated to be similar to constants described for other known iron chelators such as 2,2′-bipyridyl (pFe(III)=21.5)[41], but lower than reported for the siderophore enterobactin (pFe(III)=49)[42]. Entacapone is also predicted to complex ferrous iron (Fe(II)) with rather high affinity, but it is not predicted to form strong complexes with any other metal cations[41].

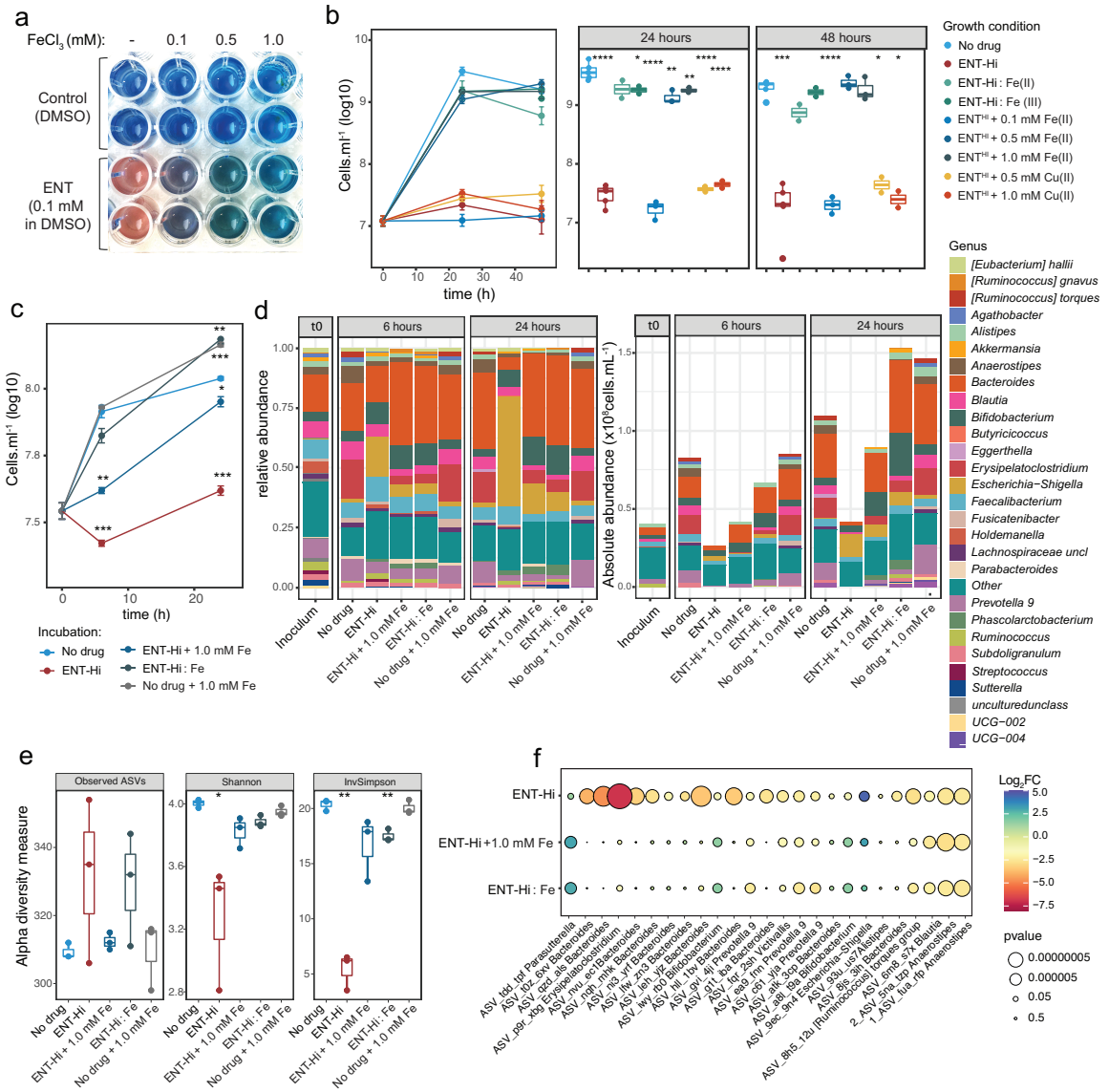

Figure 4. Iron supplementation rescues the impact of entacapone on the gut microbiome. a. Siderophore detection assay showing the change of color of the indicator complex from blue to orange/pink (see Methods) in the presence of 0.1 mM of entacapone (in DMSO), but not in the presence of DMSO alone. The indicator complex changed back to its original color (blue) after addition of an excess of ferric iron ($FeCl_3$, added at 0.1 to 1.0 mM). **b.** Growth of *Bacteroides thetaiotaomicron* in the absence of drug or in the presence of: ENT-Hi; ENT-Hi preloaded with 1 mM $FeSO_4$ (ENT-Hi:Fe(II)), ENT-Hi, ENT-Hi preloaded with 1 mM $FeCl_3$ (ENT-Hi:Fe(III)); or ENT-Hi supplemented with the indicated concentrations of Fe(II) ($FeSO_4$) or Cu(II) ($CuCl_2$)(see Methods). The box plots on the right refer to the same data as displayed on the left plot, but split by the time of incubation (24 and 48 hours), for better visualization. **c.** Total cell loads in faecal samples incubated for 6 and 24 hours with either ENT-Hi, 1mM $FeSO_4$ (No drug + 1.0 mM Fe), both (ENT-Hi + 1.0 mM Fe), or ENT-Hi pre-incubated with 1 mM of $FeSO_4$ (ENT-Hi: Fe). Total cell loads were assessed by flow cytometry. **d.** Relative (left panels) and absolute (right panels) genus abundance profiles of faecal sample microbial communities incubated as described in c and assessed by 16S rRNA gene amplicon sequencing. All genera present at relative abundances below 0.01 or absolute abundances below $1.5x10^6$ cells.ml^{-1} were assigned to the category "Other". **e.** Alpha diversity metrics (Observed ASVs, Shannon index and Inverse Simpson's diversity index) in gut microbial communities described in d. **f.** Bubble plot denoting the fold change (FC, represented as Log_2FC) in absolute abundance relative to control incubations for the 25 most abundant ASVs that are affected by ENT-Hi treatment, as assessed by DeSeq2 analyses. All ASVs have a base mean >50000, fold change of >1 or <-1 (relative no drug control), and $p_{adjusted}<0.05$. In **b**, **e** boxes represent the median, first and third quartile. Whiskers extend to the highest and lowest values that are within one and a half times the interquartile range. In **b**, **c** and **e:** *p<0.05; **p<0.01; ***p<0.001, ****p<0.0001; unpaired two-samples t-test with "No drug" used as a reference group. Only statistically significant differences are indicated.

385 Iron is a limiting nutrient in the gut and essential for growth of most gut microbes[43]. Iron
386 concentrations in stool are estimated to be around 60 μM[44], and the medium used here for
387 faecal sample incubations contained similar concentrations of iron (31 μM). As the estimated
388 concentration for entacapone in the large intestine is approximately 2 orders of magnitude
389 higher (1965 μM), we postulated that the inhibitory effect of ENT-Hi on microbial growth could
390 be directly related to its ability to deprive gut microbes from iron via chelation, similarly to what
391 has been documented for other Fe(II) and Fe(III) chelators. To test this hypothesis, we grew
392 *Bacteroides thetaiotaomicron,* a gut commensal severely impacted by Ent-Hi (log_2-fold
393 change: -4.16, adjusted p-value: 0.016, Supplementary Table 5: ASV_g1t_iba) in the
394 presence of ENT-Hi or Fe-loaded ENT-Hi (Fig.4b). Fe-loaded entacapone was obtained by
395 addition of 1 mM of Fe(II) or Fe(III) to ENT-Hi followed by removal of any excess iron cations
396 via phosphate precipitation[45] (Fig.4b; see Methods). While ENT-Hi inhibited the growth of *B.*
397 *thetaiotaomicron*, ENT-Hi pre-complexed with either Fe(III) or Fe(II) did not, enabling *B.*
398 *thetaiotaomicron* to grow normally (Fig.4b). This is in agreement with previous studies
399 reporting that supplementation of the iron chelator 2,2′-bipyridyl inhibits growth of *Bacteroides*
400 *fragilis,* but this effect is largely diminished when bipyridyl is saturated with Fe(II)[46]. This is
401 because iron-saturated chelators are no longer able to complex free Fe(II) present in the
402 medium (or intracellularly), thus enabling bacteria to access iron and grow normally. As we
403 expected iron to be mostly present in the lower oxidation state under anaerobic conditions,
404 we used Fe(II) in all subsequent incubations. Supplementation of ENT-Hi alone followed by
405 addition of increasing amounts of Fe(II) also alleviated the inhibitory effect of ENT-Hi on *B.*
406 *thetaiotaomicron*, but only when Fe(II) was added at concentrations of 0.5 mM or above
407 (Fig.4b). Addition of similar amounts of cupric (Cu(II)) ions did not reverse growth inhibition
408 by ENT-Hi (Fig.4b), confirming that the observed effect is specific for iron. In summary, these
409 results demonstrate that supplementation of Fe-salts alone or of an ENT-Hi:Fe complex
410 rescues the inhibitory effect of ENT-Hi on *B. thetaiotaomicron,* strongly indicating that
411 entacapone drives iron limitation.

412 To determine whether the results above also apply to a complex microbiota, we incubated
413 faecal samples under equivalent conditions as described in Fig.1a with ENT-Hi, ENT-Hi
414 preloaded with Fe(II) or ENT-Hi followed by addition of Fe(II). In agreement with the results
415 obtained for *B. thetaiotaomicron* alone, supplementation of the whole microbiome with iron-
416 loaded ENT-Hi or with ENT-Hi followed by 1 mM of ferrous iron resulted in a complete or near
417 complete reversal of the inhibitory effect on microbial biomass accumulation (Fig. 4c,d,
418 Supplementary Table 12). Importantly, we confirmed that this effect is not due to lower cellular
419 uptake of iron-complexed entacapone, as ENT-Hi:Fe(II) bioaccumulates in microbiota cells to
420 the same level or higher than ENT-Hi alone (Extended Data Fig.6), thus suggesting that the

421 ENT-Hi:Fe(II) complex behaves similarly to entacapone alone in terms of its ability to
422 penetrate and accumulate in cells. Supplementation of ferrous iron rescues the impact of
423 ENT-Hi on the community alpha diversity metrics as well as on the growth of nearly all of the
424 top 25 most affected taxa (exceptions are Firmicutes such as *Anaerostipes* and *Blautia*)
425 (Fig4e,f; Supplementary Tables 13 and 14). Iron supplementation does not only enable taxa
426 negatively impacted by entacapone to grow, but it also seems to restrict the accelerated
427 expansion of organisms such as *E. coli*, prompted by the presence of ENT-Hi alone (Fig.1e
428 and Fig.4d). All together these results strongly suggest that complexation of the limiting
429 nutrient iron by entacapone is the primary mechanism behind the strong inhibitory effect of
430 entacapone on the microbiome.
431
432 **Entacapone promotes growth of iron-scavenging *E. coli***

433 Next, we interrogated the capability of the few indigenous microbiome members to thrive
434 under the iron-limiting conditions induced by ENT-Hi. Several commensal and pathogenic
435 *Enterobacteriaceae*, including *E. coli*, are known to synthesize and release siderophores
436 which bind to Fe(III) with high affinity, enabling them to scavenge iron when it becomes limiting
437 and in this way, enhance their gut colonization[47]. The most dominant organism in ENT-Hi
438 incubations is an *E. coli* strain classified as *E. coli*_D (according to GTDB[48]), for which we
439 were able to recover a complete MAG (bin.187, Supplementary Table 7). A search for genes
440 involved in siderophore synthesis within the *E. coli*_D MAG led us to identify an entire gene
441 cluster coding proteins necessary for synthesis, export, and import of the siderophore
442 enterobactin (Fig.5a). Thus, we postulate that the ability of *E. coli*_D to produce enterobactin
443 enables it to grow under iron-limiting conditions induced by ENT-Hi. Indeed, after isolating this
444 *E. coli* strain from glycerol-preserved ENT-Hi incubations (isolate E2 described in methods),
445 we could confirm its ability to grow in minimal medium prepared without iron (Fig.5b). We
446 further demonstrated that its growth is not impacted (neither inhibited nor promoted) by the
447 presence of ENT-Hi when grown under isolation (Fig.5b). Enterobactin chelates ferric iron
448 with much higher efficiency than entacapone[41], and our results suggest that it enables *E. coli*
449 to scavenge and acquire enough iron to sustain its growth under the iron-limiting conditions
450 induced by the presence of entacapone (Fig.5c). The Ton-B siderophore receptor FepA may
451 also enable *E. coli* to uptake and scavenge iron from exogenous catecholate:iron
452 complexes[49], possibly even directly from iron-complexed entacapone. We could not find any
453 genes involved in the production of known siderophores in the MAG of the ENT-Hi thriving
454 *Ruminococcus*, and thus we speculate it expands in the entacapone supplemented medium
455 by importing iron-loaded siderophores produced by *E. coli*, or by producing a yet unidentified
456 siderophore or other high-affinity iron binding proteins (Fig.5c).

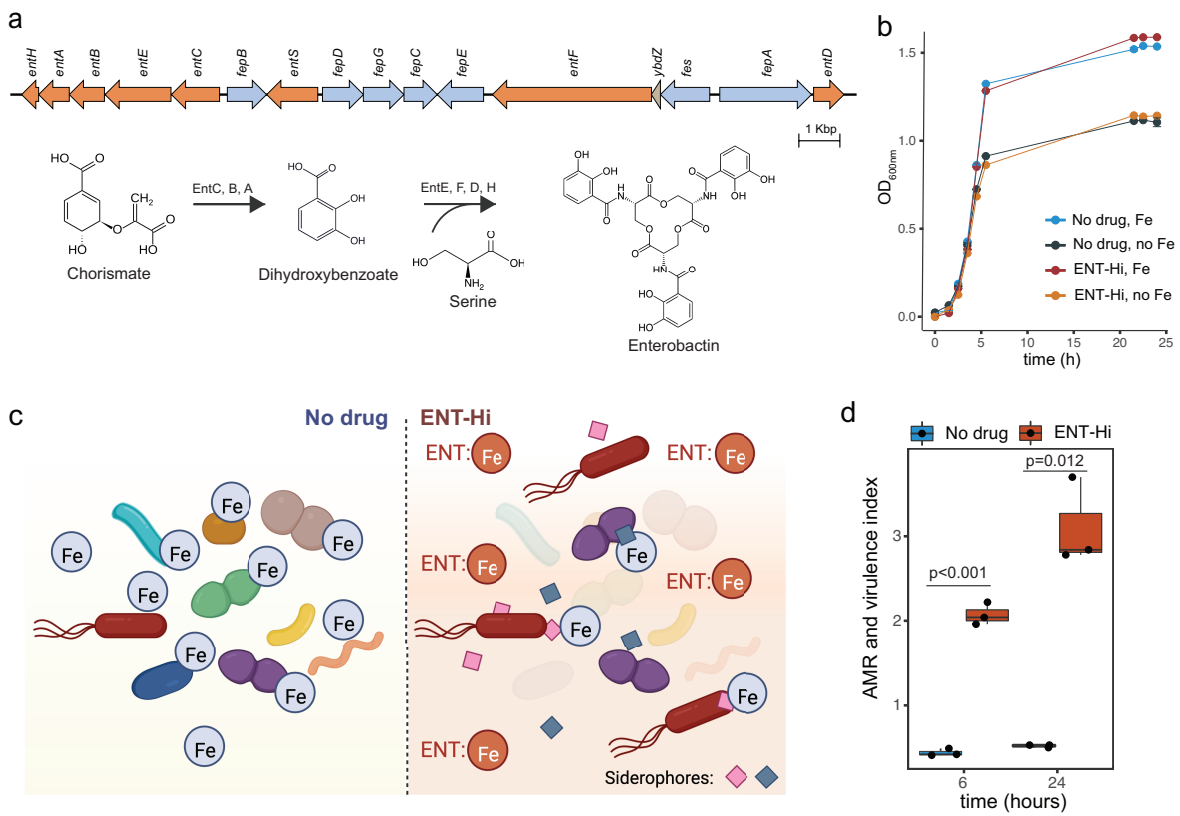

Figure 5. The iron-limiting conditions induced by entacapone select for siderophore producers and drive an increase in AMR and virulence potential in the faecal microbiome. a. Genetic organization of the enterobactin biosynthesis locus in *E. coli* D bin.187. Genes encoding enzymes involved in enterobactin biosynthesis (*entABCDEFH*) and export (*entS*) are highlighted in orange. The steps of enterobactin synthesis catalysed by the products of these genes are shown on the bottom. Genes involved in enterobactin import and iron release are highlighted in blue. **b.** Growth of an *E. coli* D bin.187 isolate determined by optical density measurements of cultures supplemented or not with 1965 μM entacapone (ENT-Hi) and/or 100 μM of $FeSO_4$. **c.** Schematic representation of the working hypothesis. In the absence of entacapone (left panel), enough iron is available to most gut microbiome members. In ENT-Hi conditions, entacapone complexes available iron (ENT:Fe), and only organisms able to produce siderophores (represented with blue and pink diamonds) for iron scavenging are able to grow and thrive (right panel). **d.** Increase in the AMR and virulence index (see Methods) in no drug controls and entacapone (ENT-Hi) treated samples. Indicated p-values were obtained from unpaired two-sample t-tests.

Siderophore production and iron scavenging are commonly observed in pathogenic or pathobiont strains that also tend to encode other virulence traits[50]. A screening of our MAG catalog for the presence of virulence factors and antimicrobial resistance genes[51] identified a diversified panel of AMR and virulence genes to be present in the retrieved gut MAGs (Supplementary Table 15), even though these samples originated from healthy individuals. These include genes encoding resistance to, among others, beta-lactams, tetracyclines, macrolides and aminoglycosides, as well as more general antimicrobial resistance genes such as efflux pumps, and virulence genes. ENT-Hi drives an increase in the abundance of AMR and virulence within faecal microbiomes (Fig.5d). This increase is driven in great part by the increase in abundance of *E. coli_D*, whose genome encodes a total of 14 AMR and virulence genes, in addition to at least one siderophore production cluster, thus suggesting a

483 pathogenic potential of this organism (Supplementary Table 15). Overall, these results reveal
484 that ENT-Hi promotes the growth of iron scavenging organisms with an associated pathogenic
485 potential.
486

487 ## Discussion

488 Gaining a deeper insight into the interactions between drugs and the gut microbiome is
489 essential for revealing and predicting how the microbiome might influence the availability,
490 efficacy and toxicity of pharmaceuticals. Here, we evaluated the impact of the nervous-system
491 targeted drugs loxapine succinate and entacapone on whole microbiomes derived from faecal
492 samples. Both drugs caused major shifts in microbial communities at physiologically relevant
493 concentrations, inhibiting the growth of many taxa while stimulating others. Using single-cell
494 activity measurements, we further revealed fine changes in the activity of specific community
495 members even at low drug concentrations and that were not captured by commonly used 16S
496 rRNA gene sequencing and abundance profiling. For instance, we did detect reduced *B.*
497 *uniformis* and *Clostridium* sp900539375 activities at 6 hours, but their abundance is not
498 affected until 24 hours (Fig.1e, Fig 2d). This is a major advantage of our approach as it
499 captures drug-induced changes in short incubation times, which are ideal for *ex vivo* systems
500 like the one in use. Importantly, our results show that loxapine succinate exerts an effect on
501 a broader range of taxa in the context of the community than its effects on microbes grown
502 under isolation[1]. This highlights the necessity of using complex microbial communities for a
503 better assessment of drug-microbiota interactions. One way by which some taxa may
504 sensitize or protect others to a particular drug is through chemical conversion or accumulation
505 of the drug[10]. However, previous studies have shown that the gut microbiota does neither
506 significantly bioaccumulate nor transform loxapine succinate[10]. Thus, we presume that cross-
507 sensitization to loxapine is likely due to drug-induced changes in microbial metabolites that
508 are involved in interspecies interactions.

509 The gut microbiome produces metabolites that can signal to the host and influence several
510 aspects of host physiology, including brain function[52]. Recent studies suggest that modulation
511 of the microbiome by drugs may contribute to the therapeutic effect of antipsychotics[1].
512 Interestingly, our results demonstrate that loxapine succinate promotes the growth of several
513 key gut species, including *Lachnospiraceae* (e.g. *Anaerostipes*) and *Butyricicoccaceae*
514 species, which have been shown to produce neuroactive metabolites such as short chain fatty
515 acids (SCFAs)[53]. SCFAs might directly or indirectly communicate along the microbiota-gut-
516 brain axis by activating G protein-coupled receptors or inhibiting histone deacetylases[54].
517 Additionally, they can modulate the blood-brain barrier, activate the vagus nerve, facilitate the

518 secretion of other hormones or neurotransmitters, as well as interfere with the immune
519 response[54], all these factors contributing to its neuromodulatory effects. Thus, it may be
520 plausible to consider changes in the microbiome as an additional mode of action of loxapine
521 succinate. This may also help to explain why it may take weeks for this antipsychotic to act
522 entirely[55], as its therapeutic effects may first require changes in the gut microbiome.

523 The impact of entacapone on the microbial community was very pronounced, selecting for the
524 growth of organisms with pathogenic potential, such as *E. coli*. An increased abundance of
525 *Enterobacteriaceae* was previously reported for Parkinson's disease (PD) patients taking
526 entacapone[56], while other studies reported increases in *Enterococcaceae, Bifidobacteriaceae*,
527 *and Clostridiales* family X[57]. These inconsistencies across studies can be partially attributed
528 to the cross-sectional and rather small number of patients involved in each study. An increase
529 in *Enterobacteriaceae* has also been linked to the side effects of other drugs[58] and may also
530 help to explain diarrhoea experienced by some patients taking entacapone. In addition,
531 entacapone is always prescribed in combination with levodopa to inhibit its off-site metabolism,
532 and frequently also in combination with carbidopa, which inhibits levodopa off-site
533 decarboxylation[27]. While levodopa has been shown to exert no effect on the distal gut
534 microbiota, probably due to its high absorption in the upper gastrointestinal (GI) tract, future
535 studies would be valuable to investigate the effects of a simultaneous supplementation of
536 entacapone and levodopa to whole microbiome communities, especially in the upper GI tract.
537 Biotic conversion of levodopa to dopamine by *Enterococcus* spp. and *Lactobacillus* spp.
538 tyrosine decarboxylases in the small intestine significantly reduces its bioavailability to the
539 host[59]. Given the strong inhibitory effect of entacapone on the microbiota, it would be
540 interesting to evaluate whether entacapone can inhibit taxa that metabolize levodopa in the
541 upper gastrointestinal tract, thereby contributing also in this way to increase the bioavailability
542 of levodopa.

543 Like levodopa, entacapone has also been shown to be metabolized by gut microbial
544 species[10]. Here, we demonstrate that entacapone is also bioaccumulated, with *Bacteroides,*
545 *Phocaeicola, Streptococcus* and *Escherichia* spp. being able to accumulate sufficient
546 amounts of entacapone for photothermal detection (Fig.3). This accumulation likely results in
547 depletion of entacapone in the surrounding environment overtime, thus explaining the slight
548 alleviation of entacapone's inhibitory effect between 6 and 24 hours of incubation, when
549 compared to the first 6 hours (Fig.1b). Interestingly, using single-cell chemical imaging we
550 further show that this bioaccumulation is heterogeneous, with some cells within a particular
551 taxon accumulating varying amounts of the drug. In addition, we further show that entacapone
552 bioaccumulation does not necessarily lead to growth inhibition (Fig.3e, f), similarly to what
553 has been described before for other bioaccumulated drugs. It remains to be determined

554 whether entacapone bioaccumulation can be linked to its metabolism. Bacterial metabolism
555 of entacapone occurs mostly by means of nitroreduction, which is prone to occur under
556 anaerobic conditions, with several *Bacteroides* spp. encoding genes linked to entacapone
557 nitroreduction[10]. Given the extensive conversion of entacapone by gut taxa observed
558 previously, we predict a large fraction of entacapone's nitrocatechol group to be in its reduced
559 form in our incubations and in the gut. Despite its bioaccumulation and/or conversion, we
560 demonstrate that entacapone exerts a strong effect on the gut community due to its ability to
561 complex iron via the catechol group.

562 Iron represents an essential enzyme cofactor in most bacteria[43]. Iron complexation by
563 entacapone led to a decrease in biomass accumulation and in the abundance of most of the
564 top abundant taxa detected in these samples, an effect that was reversed by supplementation
565 of iron (Fig.4c-f). Taxa not found to be significantly impacted by entacapone were presumably
566 able to grow by relying on intracellularly accumulated iron or on high-affinity surface-
567 associated iron transporters that are ubiquitous in bacteria. Among stimulated taxa, the
568 siderophore-producing *E. coli*_D strain present in our incubations greatly benefitted from
569 entacapone's presence, but only in the context of the community, as entacapone
570 supplementation to the isolate alone did not cause any significant boost in *E.coli*_D growth
571 (Fig.5b). Thus, taxa stimulated by entacapone likely acquired iron via the mechanisms
572 mentioned above, or via siderophores, and expanded in the community at the cost of nutrients
573 released by dead cells or supplied via cross-feeding from other species. Treatment of
574 communities with other iron complexing agents has shown somewhat similar effects on the
575 gut community[60,61].

576 The expansion of an organism with siderophore synthesis, AMR and virulence potential in the
577 presence of entacapone is concerning. Most successful gut pathogens tend to encode
578 siderophore production systems and are therefore also expected to take advantage of the
579 entacapone-induced remodeling of the gut community. It would be important to determine if
580 entacapone treatment increases the likelihood of intestinal infections, similarly to what has
581 been observed in patients taking PPIs[19]. As oral iron supplementation reduces levodopa and
582 entacapone absorption in the small intestine[62,63], the effect of entacapone on the microbiome
583 could be circumvented in the future by delivering iron specifically to the colon of patients taking
584 the drug. If administered in appropriate amounts, this new adjuvant therapy could be expected
585 to aid in preservation of microbiome homeostasis for patients taking entacapone, and
586 presumably also for patients taking other catechol-containing drugs that might reach relevant
587 concentrations in the large intestine (e.g. opicapone, apomorphine, fenoldopam mesylate) and
588 that might affect the microbiome via similar mechanisms. Colon-targeted adsorbents, such as
589 DAV132, could also be tested, as these have shown the ability to sequester antibiotic drugs

590 and reduce antibiotic-induced effects on the microbiome[64]. Our results advance our
591 understanding of the impact of antipsychotic and antidyskinetic drug therapies on microbiome
592 homeostasis, their mechanisms of action, and can direct future optimization of such therapies.
593

594 Methods

595 *Ex-vivo* gut microbiome incubations with drugs

596 Human faecal samples were collected from six healthy adult individuals (two males and four
597 females between the ages of 25 to 39) who had not received antibiotics in the prior 3 months.
598 Study participants provided informed consent and self-sampled using an adhesive paper-
599 based feces catcher (FecesCatcher, Tag Hemi, Zeijen, NL) and a sterile polypropylene tube
600 with the attached sampling spoon (Sarstedt, Nümbrecht, DE). The study protocol was
601 approved by the University of Vienna Ethics Committee (reference #00161). All meta(data) is
602 100% anonymized and compliant with the University's regulations. Samples were transferred
603 into an anaerobic tent (Coy Laboratory Products, USA) within 30 min after sampling, and all
604 sample manipulation and incubations were performed under anaerobic conditions (5% H_2,
605 10% CO_2, 85% N_2). Each sample was suspended in M9 mineral medium supplemented with
606 0.5 $mg.mL^{-1}$ D-glucose (Merck), 0.5% v/v of vitamin solution (DSMZ Medium 461) and trace
607 minerals, herein referred to as sM9. Samples were suspended in sM9 to yield a 0.05 $g.mL^{-1}$
608 faecal slurry. At this point one aliquot of each sample was collected, pelleted, and stored at -
609 80°C for metagenomic analysis. The homogenate was left to settle for 10 minutes, and the
610 supernatant (devoid of any large faecal particles) was transferred into a new flask, where
611 supernatants from the six different donors were combined. This combined sample was further
612 diluted 1:10 in sM9 medium (as described above) or in supplemented Brain Heart Infusion
613 (BHI) medium containing either 0% or 55% D_2O (99.9% atom % (at%) D; Merck) for final 0%
614 (control) or 50% D_2O in incubation medium (Fig.1a). Supplemented BHI medium consisted of
615 37 $g.L^{-1}$ of brain heart infusion broth (Oxoid), 5 $g.L^{-1}$ yeast extract (Oxoid), 1 $g.L^{-1}$ L-cysteine
616 (Merck) and 1 $g.L^{-1}$ $NaHCO_3$ (Carl Roth GmbH, Germany). Incubation tubes were
617 supplemented with dimethylsulfoxide (DMSO, from Merck), entacapone (Prestwick
618 Chemicals) or loxapine succinate (Prestwick Chemicals) pre-dissolved in DMSO. The final
619 concentration was 2% w/v of DMSO in all vials (except for the H_2O control, where water was
620 added instead of DMSO). A subset of vials was supplemented with 20 µM or 1965 µM
621 entacapone (ENT-Low and ENT-Hi, respectively) and another subset was supplemented with
622 20 µM or 100 µM loxapine succinate (LOX-Low and LOX-Hi, respectively). The colon
623 concentration estimated for entacapone is 1965 µM[1], while for loxapine no estimate was
624 available. We predicted that loxapine would reach similar colon concentrations as its chemical

625 and therapeutic analogues amoxapine and clozapine, which are estimated to reach colon
626 concentrations of 138 µM and 153 µM, respectively[1]. Using these values as a reference, we
627 predict that loxapine succinate should be present in the colon at concentrations of at least
628 100 µM and chose it as the LOX-Hi concentration. At time 0, and after an incubation time of
629 6 or 24 hours at 37°C under anaerobic conditions, two sample aliquots from each incubation
630 and controls were collected by centrifugation. One aliquot was washed with 1× PBS and then
631 fixed in 3% paraformaldehyde solution for 2 h at 4°C. Samples were finally washed two times
632 with 1 ml of PBS and stored in PBS:Ethanol (50% v/v) at -20°C until further use. The second
633 pelleted aliquot was stored at -20°C until further processing. A third aliquot was collected into
634 sealed anaerobic vials containing 40% glycerol (Carl Roth GmbH, Germany) in PBS for a final
635 cell 50% v/v cell suspension in 20% glycerol and stored at -80°C until further use.

636 For iron rescue experiments, fresh faecal samples received from the same individuals (except
637 for one male that was traveling at the time of the experiment) were collected and processed
638 as described above. To establish appropriate controls for imaging of entacapone
639 bioaccumulation by microbiota cells, an aliquot of the freshly prepared 0.05 $g.mL^{-1}$ faecal
640 slurry was immediately fixed with either 3% PFA solution or ethanol (50% v/v) at 4°C for 2
641 hours. Fixed faecal samples were washed with 1xPBS as described above and incubations
642 with fixed samples and entacapone or entacapone:iron (see below) were conducted in parallel
643 with incubations using live samples. Incubation vials were then supplemented with DMSO 2%
644 v/v with or without 1965 µM entacapone, in the presence or absence of supplemented iron
645 (1mM $FeSO_4$, Merck; Fig.5). Additional incubation vials (triplicates) were treated with
646 entacapone pre-complexed with iron: briefly, entacapone and iron ($FeSO_4$ or $FeCl_3$) powder
647 were mixed and resuspended in 2 mL of DMSO yielding a final concentration of 1965 µM
648 entacapone and 1 mM $FeSO_4$ (or $FeCl_3$) and stored overnight under anaerobic conditions.
649 The next day, 120µL of sodium phosphate monobasic (0.5M) was added and the samples
650 were mixed well. After 20 minutes, samples were centrifuged for 5 min, 14000 *g* to remove
651 unbound iron precipitated by the addition of sodium phosphate[45]. The supernatant containing
652 the iron-complexed entacapone was collected into a new eppendorf tube and supplemented
653 to the faecal incubation vials. Incubations were sampled as described above.
654

655 **Cell counts from *ex-vivo* microbiome incubations**

656 Microbial loads in faecal incubation vials were determined using flow cytometry and counting
657 beads as detailed below. Samples preserved in glycerol were diluted 200 to 800 times in 1x
658 PBS (Supplementary Table 1). To remove any additional debris from the faecal incubations,
659 samples were transferred into a flow cytometry tube by passing the sample through a snap
660 cap containing a 35 µm pore size nylon mesh. Next, 500 µL of the microbial cell suspension

661 was stained with the nucleic acid dye SYTO™ 9 (Thermo Fisher Scientific, 0.5 μM in DMSO)
662 for 15 min in the dark. The flow cytometry analysis of the microbial cells present in the
663 suspension was performed using a BD FACSMelody™ (BD Biosciences), equipped with a BD
664 FACSChorus™ software (BD). Briefly, background signals from the instrument and the buffer
665 solution (PBS) were identified using the operational parameters forward scatter (FSC) and
666 side scatter (SSC). Microbial cells were then displayed using the same settings in a scatter
667 plot using the forward scatter (FSC) and side scatter (SSC) and pre-gated based on the
668 presence of SYTO™ 9 signals. Singlets discrimination was performed. Absolute counting
669 beads (CountBright™, ThermoFisher Scientific) added to each sample were used to determine
670 the number of cells per mL of culture by following the manufacturer's instructions.
671 Fluorescence signals were detected using the blue (488 nm – staining with SYTO™ 9 and
672 CountBright™ beads) and yellow-green (561 nm - CountBright™ beads only) optical lasers.
673 The gated fluorescence signal events were evaluated on the forward–sideways density plot,
674 to exclude remaining background events and to obtain an accurate microbial cell count
675 (Supplementary Table 1). Instrument and gating settings were identical for all samples (fixed
676 staining–gating strategy).
677
678 **Nucleic acid isolation and 16S rRNA gene amplification and sequencing**

679 Pellets of microbiome incubation samples were resuspended in 600 μl of lysis solution RL
680 (InnuPREP DNA/RNA mini kit, Analytik Jena) and subjected to bead beating for 30 seconds
681 at 6.5 m/s in lysis matrix E (MPBiomedicals) tubes. After pelleting cell debris for 10 minutes
682 at 8000g, supernatants were transferred into the InnuPREP DNA/RNA mini kit spin filter tubes
683 (Analytik Jena) and DNA and RNA were extracted according to the manufacturer's protocol.
684 Amplification of bacterial and archaeal 16S rRNA genes from DNA extracts was performed
685 with a two-step barcoding approach[65] (UDB-H12).

686 In the first-step PCR, the primers 515F[66] (5′-GTGYCAGCMGCCGCGGTAA-3′) and 806R[67]
687 (5′-GGACTACNVGGGTWTCTAAT-3′), including a 5′-head sequence for 2-step PCR
688 barcoding, were used. PCRs, barcoding, library preparation and Illumina MiSeq sequencing
689 were performed by the Joint Microbiome Facility (Vienna, Austria) under project numbers
690 JMF-2208-05 and JMF-2103-29. First-step PCRs were performed in triplicate (12.5 μl vol per
691 reaction) with the following conditions: 1X DreamTaq Buffer (Thermo Fisher), 2 mM MgCl2
692 (Thermo Fisher), 0.2 mM dNTP mix (Thermo Fisher), 0.2 μM of forward and reverse primer
693 each, 0.08 mg ml−1 Bovine Serum Albumin (Thermo Fisher), 0.02 U Dream Taq Polymerase
694 (Thermo Fisher), and 0.5 μl of DNA template. Conditions for thermal cycling were: 95°C for
695 3 min, followed by 30 cycles of 30 s at 95°C, 30 s at 52°C and 50 s at 72°C, and finally 10 min
696 at 72°C. Triplicates were combined for barcoding (with eight PCR cycles). Barcoded samples

697 were purified and normalized over a SequalPrep Normalization Plate Kit (Invitrogen) using a
698 Biomek NXP Span-8 pipetting robot (Beckman Coulter), and pooled and concentrated on
699 PCR purification columns (Analytik Jena). Indexed sequencing libraries were prepared with
700 the Illumina TruSeq Nano Kit as described previously[68], and sequenced in paired-end mode
701 (2× 300 bp; v3 chemistry) on an Illumina MiSeq following the manufacturer's instructions. The
702 workflow systematically included four negative controls (PCR blanks, i.e., PCR-grade water
703 as template) for each 90 samples sequenced. The 16S rRNA gene sequences were deposited
704 in the NCBI Sequence Read Archive (SRA) as BioProject Accession PRJNA1033532.
705

706 **Analysis of 16S rRNA gene amplicon sequences**

707 Amplicon pools were extracted from the raw sequencing data using the FASTQ workflow in
708 BaseSpace (Illumina) with default parameters[65]. Demultiplexing was performed with the
709 python package demultiplex (Laros JFJ, github.com/jfjlaros/demultiplex) allowing one
710 mismatch for barcodes and two mismatches for linkers and primers. DADA2[69] R package
711 version 1.16.0 (https://www.r-project.org/, R 4.0.2) was used for demultiplexing amplicon
712 sequencing variants (ASVs) using a previously described standard protocol[70]. FASTQ reads
713 were trimmed at 150 nt with allowed expected errors of 2. Taxonomy was assigned to 16S
714 rRNA gene sequences based on SILVA taxonomy[71] (release 138) using the DADA2 classifier.

715 Samples were analyzed using the vegan (v2.5-.6; https://CRAN.R-
716 project.org/package=vegan) and phyloseq[72] (v1.30.0) packages of the software R
717 (https://www.r-project.org/, R 4.0.2). For samples subjected to different drug treatments,
718 sequencing in parallel of two extraction controls (without adding faecal samples) yielded 10
719 (control 1) and 189 reads (control 2). In control 1, 9 of the 10 reads were assigned to
720 Cyanobacteria or chloroplast and were not detected in the samples. Likewise, in control 2,
721 more than 90% of the reads originated from either Cyanobacteria ASVs or a single
722 Comamonadaceae (*Aquabacterium*) not detected in any of the samples. These ASVs were
723 removed from analysis. The remaining negative control reads (control 1: 1 read, control 2: 8
724 reads) were assigned to taxa typically found in the gut that were also detected in the samples
725 and were therefore retained for subsequent analyses. We assume these low number of reads
726 to originate from a low level of cross-contamination that can occur when multiple samples are
727 handled in parallel. After quality filtering and removal of contaminant sequences, a total of
728 1132 ASVs were retained. The average read number per sample was 11176 ± 3087 high-
729 quality sequences, and sample coverage was above 98% (Supplementary Table 2). For alpha
730 and beta diversity analysis, sequence libraries were rarefied to 4681 reads per sample. For
731 samples referring to the entacapone and iron supplementation experiment, sequencing in
732 parallel of two extraction controls yielded 2 (control 1) and 134 reads (control 2). After quality

733 filtering and removal of contaminant sequences (using the rationale described above), a total
734 of 716 ASVs were retained. The average read number per sample was 18733 ± 4427 high-
735 quality sequences and the sample coverage was above 99% (Supplementary Table 2). For
736 alpha diversity analysis, sequence libraries were rarefied to 9729 reads per sample. For
737 quantitative microbiome analyses, relative abundances of each taxon in a sample were
738 calculated after correcting for the different number of copies of the 16S rRNA gene, according
739 to *rrn*DB (version 5.7). For this correction, we classified ASVs using DADA2 and the RDP[73]
740 taxonomy 18, release 11.5 (https://doi.org/10.5281/zenodo.4310151), by applying default
741 parameters. These corrected relative abundances were then multiplied by the total microbial
742 loads obtained from flow cytometry (Supplementary Table 1), yielding the total abundance of
743 each taxon per sample.

744 DESeq2[74] (v1.26.0) implemented in phyloseq was used to identify significant differences in
745 ASV abundances between drug treatments. Only ASVs that had in total ≥10 reads (relative
746 abundance microbial profile) or 5.0e5 reads (quantitative microbial profile) were considered
747 for comparisons by DESeq2 analyses. All statistical analysis of microbiome data was carried
748 out with the software R (R 4.0.2). The applied significance tests and obtained p-values are
749 referred to in the main text and figure legends.
750
751 **Long-read sequencing**

752 DNA for long-read sequencing was isolated using the DNeasy PowerSoil Pro Kit (Qiagen),
753 according to the manufacturer's instructions. A pool of 6 DNA extracts was prepared for
754 sequencing using the ligation sequencing kit (SQK-LSK112, Oxford Nanopore Technologies)
755 following the manufacturer's protocol. The DNA was sequenced on a Promethion P24 (Oxford
756 Nanopore Technologies) on a R10.4 flowcell (FLO-PRO112, Oxford Nanopore
757 Technologies). The DNA sequencing was carried out using Minknow (v. 21.10.8, Oxford
758 Nanopore Technologies).
759
760 **Shotgun metagenomic sequencing**

761 The same 6 samples were individually sequenced in an Illumina Novaseq 6000 platform by
762 the Joint Microbiome Facility (Vienna, Austria), under project number JMF-2110-04. The
763 illumina reads were trimmed using cutadapt[75] (v. 3.1). Illumina reads were mapped to the
764 assemblies using Minimap2[76] (v. 2.17).
765
766 **Metagenomic analysis**

767 The Nanopore reads were assembled using flye[77] (v. 2.9-b1768) with "–nano-hq," polished
768 three times with Minimap2[76] (v. 2.17) and Racon[78] (v. 1.4.3), followed by two rounds of

769 polishing with Medaka (v. 1.4.4, github.com/nanoporetech/medaka). Illumina and Nanopore
770 reads (Supplementary Table 6) were mapped to the assemblies using Minimap2 (v. 2.17) and
771 read mappings were converted using SAMtools[79] (v. 1.12). Read coverage and automatic
772 binning was performed using MetaBAT2[80] (v. 2.15). Contigs labeled as circular by the
773 assembler were extracted as independent bins before the automated binning process. The
774 quality of the recovered metagenome-assembled genomes (MAGs) was checked using
775 QUAST[81] (v. 5.0.2) and CheckM[82] (v. 1.1.1), and genomes were classified using GTDBtk[48] (v.
776 1.5.1). rRNA genes were detected using Barrnap (v. 0.9,
777 https://github.com/tseemann/barrnap.) and tRNA genes were detected using trnascan[83] (v.
778 2.0.6). MAGs with a completeness >90 % but where barrnap did not pick up a 5S rRNA gene
779 were checked for 5S rRNA genes using INFERNAL[84] (v. 1.1.3).

780 All MAGs were searched for anti-microbial resistance (AMR) and virulence genes using
781 AMRFinderPlus[51] (v.3.10.21). The AMR and virulence index (Fig.5a) was calculated as
782 follows: the total copies of AMR and virulence genes found to be present in each MAG were
783 multiplied by the absolute abundance of the MAG (abundance of the ASV matching the 16S
784 rRNA gene of the MAG) in the sample. The same was repeated for all MAGs for which
785 AMRFinderPlus identified AMR or virulence genes and by summing these we were able to
786 predict the total number of copies of AMR and virulence genes for each sample, per mL of
787 culture. The resulting values were then normalized to the total biomass per mL of each sample
788 in order to obtain an AMR and virulence index per sample.

789

790 **FISH probe design and optimization**

791 Phylogenetic analysis and FISH probe design were performed using the software ARB v. 7.0[85].
792 By analysis of the 16S and 23S rRNA gene, phylogenetic trees were calculated with IQ-
793 TREE[86] (v 1.6.12) using the RAxML GTR algorithm with 1,000 bootstraps within ARB. For
794 abundant groups, 4 FISH probes were designed for this study and 2 additional published
795 probes were used (Supplementary Table 9). The probes were validated *in silico* with
796 mathFISH to test the *in-silico* hybridization efficiency of target and non-target sequences. The
797 number of non-target sequences was assessed using the probe match function in ARB and
798 the mismatch analysis function in mathFISH. All probes were purchased from biomers
799 (Biomers.net, Ulm, Germany) and were double labeled with indocarbocyanine (Cy3) or sulfo-
800 cyanine5 (Cy5) fluorochromes.

801 Pure cultures of *Escherichia coli* K-12, *Phocaeicola dorei* 175 (DSM17855) and *Bacteroides*
802 *thetaiotaomicron* VPI-5482 (DSM2079) were grown in supplemented BHI until the mid-
803 exponential phase and harvested by centrifugation. Pure cultures were fixed for 2 h by addition

804 of 3 volumes of 4% (w/v) paraformaldehyde solution at 4 °C. After washing once with PBS,
805 cells were stored in a 1:1 mixture of PBS and 96% (v/v) ethanol at − 20 °C. Where pure
806 cultures were not available, fixed faecal samples with a high relative abundance (as
807 determined by amplicon sequencing) of the specific target taxon was used.

808 To evaluate probe dissociation profiles, cells obtained from fixed pure cultures or faecal
809 incubation samples (Supplementary Table 9) were spotted onto microscopy slides (Paul
810 Marienfeld EN). FISH was performed as described before[87,88], with 3 or 5h hybridization to
811 obtain fluorescence signals with sufficient intensity. The optimal hybridization formamide
812 concentration was found using formamide dissociation curves, obtained by application of
813 formamide concentration series in the range from 0 to 70% in 5% increments[89]. After a
814 stringent washing step and counterstaining using 4′,6-diamidino-2-phenylindole, samples
815 were visualized using a Leica Thunder Epifluorescence microscope with an APO 100x/1,40
816 Leica oil immersion objective. Probe EUB338[90], which is complementary to a region of the
817 16S rRNA conserved in many members of the domain Bacteria, was used as a positive control
818 and a nonsense NON-EUB probe was applied to samples as a negative control for binding.
819 Images for inferring probe dissociation profiles were recorded using the same microscopy
820 settings and exposure times. The probe dissociation profiles were determined based on the
821 mean fluorescence signal intensities of at least 100 probe-labeled cells and evaluated by the
822 ImageJ software (v 1.53t). From the calculated average values, a curve was plotted and the
823 respective value right before a decline on each curve was defined as the optimal formamide
824 concentration.
825

826 **FISH in solution**

827 Fixed cells (100 µl) were pelleted at 14000 *g* for 10 min, resuspended in 100 µl 96% analytical
828 grade ethanol and incubated for 1 min at room temperature for dehydration. Subsequently,
829 the samples were centrifuged at 14000*g* for 5 min, the ethanol was removed, and the cell
830 pellet was air-dried. For SRS-FISH analysis, cells were hybridized in solution (100 µl) for 3 h
831 at 46°C. The hybridization buffer consisted of 900 mM NaCl, 20 mM TRIS HCl, 1 mM EDTA,
832 0.01% SDS and contained 100 ng of the respective fluorescently labelled oligonucleotide as
833 well as the required formamide concentration to obtain stringent conditions (Supplementary
834 Table 9). After hybridization, samples were immediately transferred into a centrifuge with a
835 rotor pre-heated at 46°C and centrifuged at 14000 *g* for 15 min at maximum allowed
836 temperature (40°C), to minimize unspecific probe binding. Samples were washed in a buffer
837 of appropriate stringency for 15 min at 48°C, cells were centrifuged for 15 min at 14 000 g
838 and finally resuspended in 20 µl of PBS. Cells (5 µl) were spotted on Poly-L-lysine coated

839 cover glasses No. 1.5H (thickness of 170 µm ± 5 µm, Paul Marienfeld EN) and allowed to dry
840 overnight at 4°C under protection from light. Salt precipitates were removed by dipping the
841 coverslips 2× in ice-cold Milli-Q water and allowed to dry at room temperature under protection
842 from light.
843

844 **Picosecond stimulated Raman scattering (SRS) with widefield fluorescence**
845 **microscopy**

846 An 80-MHz pulsed laser (InSight DeepSee+; Spectra-Physics) emitting two synchronized
847 femtosecond beams was used (Extended Data Fig.2a). One beam was tunable in wavelength
848 from 680 nm to 1300 nm, while the other beam had a fixed wavelength of 1040 nm. The time
849 delay between single pulses of the two beams is adjustable by a motorized delay line on the
850 1040 nm beam. To implement the picosecond stimulated Raman scattering (SRS) (Extended
851 Data Fig.2), the fixed beam (termed Stokes beam) is intensity modulated at 2.5 MHz by an
852 acousto-optic modulator (1205c; Isomet Corporation) and co-aligned with the tunable beam
853 (termed pump beam), by a dichroic mirror (DMLP1000; Thorlabs). Both beams are chirped by
854 SF57 rods to two picoseconds pulse-width and directed towards the lab-built upright
855 microscope frame. Then, a four-focal system and a flip mirror conjugate a pair of galvo mirrors
856 to the back aperture of a 60× water objective (UPlanApo 60XW, numerical aperture = 1.2;
857 Olympus) or a 100× oil objective (UAPON 100XOTIRF, numerical aperture = 1.49; Olympus),
858 allowing the collinear pump and Stokes beams to raster-scan the sample via synchronized
859 movement of the galvo mirrors. A 1.4 numerical aperture oil condenser (Aplanat Achromat
860 1.4; Olympus) collects the output beams, which are then reflected by a flip mirror and filtered
861 by a short pass filter (DMSP950; Thorlabs). Finally, the filtered-out pump beam is focused
862 onto a silicon photodiode connected to a resonant amplifier effective at a resonant frequency
863 around 2.5 MHz. The output alternative current signal is further amplified by a lock-in amplifier
864 (UHFLI; Zurich Instrument) at the frequency and in phase (x channel detection) with the
865 modulation. The output direct current signal is recorded for normalization. A data acquisition
866 card (PCIe-6363; National Instruments) collects the output signal for image generation.

867 To perform widefield fluorescence imaging for FISH-visualization of the identical sample areas
868 analyzed by SRS and photothermal imaging, two flip mirrors were flipped off (Extended Data
869 Fig.2a). A halogen lamp (12V100WHAL; Olympus) provides Kohler illumination of the sample
870 from the condenser side. Then, the objective and the tube lens conjugate the sample plane
871 to the camera (CS505CU; Thorlabs). To enable imaging of various fluorophores, different
872 excitation and emission filter sets were inserted between lamp and condenser, and in front of
873 the camera. For Cy3 imaging, two 530/10 nm bandpass filters (FBH530-10; Thorlabs) were
874 used as excitation filters and two 570/20 nm bandpass filters (ET570/20x; Chroma) were used

875 as emission filters. For Cy5 imaging, two 640 nm bandpass filters (FBH640-10; Thorlabs)
876 were used as excitation filters and two 670/20 nm bandpass filters (ET670/50m; Chroma)
877 were used as emission filters.
878
879 **Chemical imaging of entacapone accumulation**

880 By utilizing the multiphoton absorption of entacapone, we detected the photothermal signal
881 originating from optical absorption to generate entacapone distribution maps. The
882 experimental setup was identical with picosecond SRS, but with detection of the lock-in signal
883 by the y channel, which exhibits a π/2 phase delay relative to the intensity modulation by the
884 AOM (Extended Data Fig.4b). With this orthogonal phase detection, the interference of the
885 photothermal signal with the signals emerging from cross-phase modulation and SRS was
886 minimized (Extended Data Fig.4d).
887
888 **Image acquisition and processing**

889 Samples were prepared by drying fixed bacterial cells spotted onto poly-L-lysine coated
890 coverslips (VistaVision cover glasses, No. 1; VWR) in a 4°C refrigerator and subsequent
891 dipping into water three times to dissolve precipitates from the growth media. Then the
892 bacteria were immersed in 5 µL of water and sandwiched by another coverslip with a 0.11
893 mm thick spacer in between. To acquire deuterium incorporation profiles of microbiome
894 members labeled by FISH probes, widefield fluorescence was performed first. For different
895 fluorophores, corresponding excitation and emission filters were applied. The signal and color
896 gain of the camera were set to 5. Then the exposure time was adjusted to 0.5 to 5 seconds
897 depending on the fluorescence signal intensity. The widefield transmission image was
898 acquired by minimizing the condenser aperture and removing the filters.

899 To acquire the deuterium incorporation profile of the FISH-visualized cells, two flip mirrors
900 were inserted into the beam path to guide the pump and Stokes lasers to the sample. Three
901 SRS images, specific for Raman active vibrational modes of carbon-deuterium (C-D) bonds,
902 carbon-hydrogen (C-H) bonds as well as the off-resonance background signal were recorded
903 by tuning the wavelength of the pump beam to 849 nm, 796 nm and 830 nm, respectively.
904 These wavelength values correspond to spectral wavenumbers of 2163 cm^{-1} (C-D), 2947 cm^{-}
905 ^{1} (C-H) and 2433 cm^{-1} (silent region). Signal intensities were accumulated over increments of
906 20 cm^{-1}. Images were acquired sequentially within the identical field of view of 32 x 32 μm^2
907 with a raster step size of 106.8 nm. The per-pixel dwell time was set to 10 µs and, depending
908 on the signal intensity level, 1~10 image cycles were recorded to achieve a signal-to-noise
909 ratio (SNR) of >5 for single bacterial cells in the C-H spectral region.

910 For acquisition of entacapone distribution maps, the pump laser was tuned to 849 nm and the
911 signal detection was switched to the y channel of the lock-in amplifier. All images were
912 recorded utilizing the identical scanning parameters as applied for SRS.

913 To process the image data sets, firstly, the illumination patterns were corrected for both
914 widefield images (FISH) and point-scan images (SRS and entacapone distribution). Then, the
915 widefield images and point-scan images were co-localized via a calibrated projective
916 transform matrix. The fluorescence images were utilized to generate a single cell mask for
917 inference of the single cell activity and the drug accumulation level. The single cell activity is
918 expressed as $\%CD_{SRS} = (I_{CD}-I_{off})/(I_{CD}+I_{CH}-2I_{off})$, where the symbols I_{CD}, ICH and I_{off} refer to the
919 SRS signal intensities detected at the spectral positions assigned to C-D bonds, C-H bonds
920 and the silent region (off-resonance background). All intensity values were normalized to the
921 direct current intensity level detected at the photodiode. The relative entacapone
922 accumulation level is expressed as the signal intensity level detected in the y channel of the
923 lock-in amplifier. intensity outliers (>mean±2 standard deviations) observed in the SRS signals
924 and the photothermal signal of the human gut microbiome samples, were rejected from the
925 single cell masks. All imaging data analysis was performed with CellProfiler and Matlab.
926

927 **Siderophore assay**

928 The iron binding capacity of entacapone was tested using the SideroTec Assay™ (Accuplex
929 Diagnostics, Ireland), a colorimetric test for the detection of siderophores, according to the
930 manufacturer's instructions. Wells were read photographically and on a microplate reader at
931 630 nm wavelength (MultiskanTM GO Microplate Spectrophotometer, Thermo Fisher
932 Scientific).
933

934 **Isolation and sequencing of *Escherichia coli* human gut isolate**

935 *Escherichia coli* isolate E2 was isolated from glycerol-preserved faecal samples after
936 incubation in sM9 medium supplemented with 1965 µM entacapone for 48 hours under
937 anaerobic conditions. An aliquot of the glycerol stock was serially diluted in PBS, and 10^{-4} and
938 10^{-5} dilutions were plated in BHIs agar. Isolated colonies were re-streak 3 times to purity and
939 submitted to colony PCR using the 16S rRNA gene primers 616V (5'- AGA GTT TGA TYM
940 TGG CTC AG-3') and 1492R (5'- GGT TAC CTT GTT ACG ACT T -3'). Single colonies were
941 picked with an inoculation loop, resuspended in 50 µl of nuclease free water and boiled at
942 95°C for 10 minutes to lyse the cells and release cell contents. After a short spin to pellet cell
943 debris, 2 µl of the supernatant was added to a PCR reaction mix (final concentrations; Green
944 1X Dream Taq Buffer, dNTPs 0.2 mM, BSA 0.2 mg/ml, Taq polymerase 0.05 U/µl, primers 1
945 µM) prepared in a final volume of 50 µl per reaction. The amplification cycles were as follow:

946 initial denaturation at 95 °C for 3 min, followed by 30 cycles at 95 °C for 30 s, 52 °C for 30 s,
947 72 °C for 1.5 min, and a final elongation at 72 °C for 10 min. PCR products were visualized
948 on 1.5% agarose gel electrophoresis, and subsequently cleaned and concentrated on
949 columns (innuPREP PCRpure Kit, Analytik Jena) according to the manufacturer´s
950 instructions. Concentrations were measured by Nanodrop, and samples were sent for Sanger
951 sequencing at Microsynth AG (Vienna, Austria). Sequencing results were analyzed by
952 BLASTn[32] against the 16S rRNA gene sequences retrieved by metagenomics. The near full
953 16S rRNA gene sequences of isolate E2 obtained were 99% identical to the 16S rRNA copies
954 of *E. coli* D bin.187 and 100% identical to ASV_9ec_9n4.
955

956 **Growth of microbial pure cultures in the presence of entacapone and/or iron**

957 *Bacteroides thetaiotaomicron* (DSM 2079) cells were grown anaerobically (85% N_2, 10% CO_2,
958 5% H_2) at 37°C in *Bacteroides* minimal medium (BMM) containing 27.5 µM of iron ($FeSO_4$,
959 Merck)[91]. To test the effect of iron on rescuing the inhibitory effect of entacapone on *B.*
960 *thetaiotaomicron* growth, entacapone-treated (1965 µM) cultures were supplemented with
961 100 µM, 500 µM or 1mM of iron. Growth rescue was observed when cultures were
962 supplemented with either 500 µM $FeSO_4$ (Fe(II)) or $FeCl_3$ (Fe(III)), and for all subsequent
963 experiments only $FeSO_4$ was used. Cu(II)SO_4 (500 µM or 1mM - Merck) or entacapone pre-
964 complexed with iron (1965 µM, prepared as described above) were also supplemented to *B.*
965 *thetaiotaomicron* cultures. Samples for total cell counts were taken at 0, 24, and 48 hours of
966 growth under anaerobic conditions. *Phocaeicola dorei* (DSM 17855) was grown in BMM in
967 the presence or absence of 1965 µM entacapone. After 24 and 48 hours of growth, an aliquot
968 was collected and fixed with paraformaldehyde as described above, and stored at -20°C in
969 PBS:EtOH 50% v/v until further analyses. To test if growth of the *Escherichia coli* faecal isolate
970 E2 was dependent on the presence of iron, the isolate was grown in MOPS medium without
971 or without 10 µM of $FeSO_4$ in the presence or absence of entacapone for 24 hours at 37°C.
972 To avoid the transfer of any iron from the pre-inoculum, pre-inoculum cells were washed
973 thoroughly in MOPS medium without iron, prior to inoculation.
974

975 **Determination of total cell loads in pure cultures incubated with entacapone and iron**

976 To determine microbial cell loads in pure culture, samples were collected at 0, 24 or 48 hours
977 of growth and stained (either undiluted or after a dilution of 10 times in 1x PBS) with the
978 QUANTOM™ Total Cell Staining Kit (Logos Biosystems, Korea). Total cell counts were
979 determined using a QUANTOM Tx™ Microbial Cell Counter (Logos Biosystems, Korea),
980 according to the manufacturer's instructions.
981

Data availability

The 16S rRNA gene sequences data have been deposited in the National Center for Biotechnology Information (NCBI) Sequence Read Archive (accession number PRJNA1033532).

Code availability

CellProfiler pipelines and Matlab codes have been deposited in GitHub (https://github.com/buchenglab/srs-fish-drugs).

References

1. Maier, L. *et al.* Extensive impact of non-antibiotic drugs on human gut bacteria. *Nature* **555**, 623–628 (2018).
2. Weersma, R. K., Zhernakova, A. & Fu, J. Interaction between drugs and the gut microbiome. *Gut* **69**, 1510–1519 (2020).
3. Lynch, S. V. & Pedersen, O. The human intestinal microbiome in health and disease. *N Engl J Med* **375**, 2369–2379 (2016).
4. Falony, G. *et al.* Population-level analysis of gut microbiome variation. *Science* **352**, 560–564 (2016).
5. Zhernakova, A. *et al.* Population-based metagenomics analysis reveals markers for gut microbiome composition and diversity. *Science* **352**, 565–569 (2016).
6. Jackson, M. A. *et al.* Gut microbiota associations with common diseases and prescription medications in a population-based cohort. *Nat Commun* **9**, 2655 (2018).
7. Vich Vila, A. *et al.* Impact of commonly used drugs on the composition and metabolic function of the gut microbiota. *Nat Commun* **11**, 362 (2020).
8. Li, L. *et al.* RapidAIM: a culture- and metaproteomics-based Rapid Assay of Individual Microbiome responses to drugs. *Microbiome* **8**, 33 (2020).
9. Zimmermann, M., Zimmermann-Kogadeeva, M., Wegmann, R. & Goodman, A. L. Separating host and microbiome contributions to drug pharmacokinetics and toxicity. *Science* **363**, eaat9931 (2019).
10. Zimmermann, M., Zimmermann-Kogadeeva, M., Wegmann, R. & Goodman, A. L. Mapping human microbiome drug metabolism by gut bacteria and their genes. *Nature* **570**, 462–467 (2019).
11. van Kessel, S. P., Bullock, A., van Dijk, G. & El Aidy, S. Parkinson's disease medication alters small intestinal motility and microbiota composition in healthy rats. *mSystems* **7**, e01191-21 (2022).
12. Wallace, B. D. *et al.* Alleviating cancer drug toxicity by inhibiting a bacterial enzyme. *Science* **330**, 831–835 (2010).
13. Klünemann, M. *et al.* Bioaccumulation of therapeutic drugs by human gut bacteria. *Nature* **597**, 533–538 (2021).
14. Tropini, C. *et al.* Transient osmotic perturbation causes long-term alteration to the gut microbiota. *Cell* **173**, 1742-1754.e17 (2018).
15. Fung, T. C. *et al.* Intestinal serotonin and fluoxetine exposure modulate bacterial colonization in the gut. *Nat Microbiol* **4**, 2064–2073 (2019).
16. Bhatt, A. P. *et al.* Targeted inhibition of gut bacterial β-glucuronidase activity enhances anticancer drug efficacy. *Proc Natl Acad Sci USA* **117**, 7374–7381 (2020).
17. Wu, H. *et al.* Metformin alters the gut microbiome of individuals with treatment-naive type 2 diabetes, contributing to the therapeutic effects of the drug. *Nat Med* **23**, 850–858 (2017).

1029 18. Sun, L. *et al.* Gut microbiota and intestinal FXR mediate the clinical benefits of metformin.
1030 *Nat Med* **24**, 1919–1929 (2018).
1031 19. Jackson, M. A. *et al.* Proton pump inhibitors alter the composition of the gut microbiota.
1032 *Gut* **65**, 749–756 (2016).
1033 20. Buffie, C. G. & Pamer, E. G. Microbiota-mediated colonization resistance against intestinal
1034 pathogens. *Nat Rev Immunol* **13**, 790–801 (2013).
1035 21. Stark, C. M., Susi, A., Emerick, J. & Nylund, C. M. Antibiotic and acid-suppression
1036 medications during early childhood are associated with obesity. *Gut* **68**, 62–69 (2019).
1037 22. Ait Chait, Y., Mottawea, W., Tompkins, T. A. & Hammami, R. Unravelling the antimicrobial
1038 action of antidepressants on gut commensal microbes. *Sci Rep* **10**, 17878 (2020).
1039 23. Cussotto, S. *et al.* Differential effects of psychotropic drugs on microbiome composition
1040 and gastrointestinal function. *Psychopharmacology* **236**, 1671–1685 (2019).
1041 24. Zhang, W., Qu, W., Wang, H. & Yan, H. Antidepressants fluoxetine and amitriptyline
1042 induce alterations in intestinal microbiota and gut microbiome function in rats exposed to
1043 chronic unpredictable mild stress. *Transl Psychiatry* **11**, 1–16 (2021).
1044 25. Fang, P., Kazmi, S. A., Jameson, K. G. & Hsiao, E. Y. The microbiome as a modifier of
1045 neurodegenerative disease risk. *Cell Host Microbe* **28**, 201–222 (2020).
1046 26. Pratt, L. A., Brody, D. J. & Gu, Q. Antidepressant use among persons aged 12 and
1047 over:United States,2011-2014. *NCHS Data Brief* 1–8 (2017).
1048 27. Myllylä, V. V., Sotaniemi, K. A., Illi, A., Suominen, K. & Keränen, T. Effect of entacapone,
1049 a COMT inhibitor, on the pharmacokinetics of levodopa and on cardiovascular responses
1050 in patients with Parkinson's disease. *Eur J Clin Pharmacol* **45**, 419–423 (1993).
1051 28. Schiele, B. C. Loxapine succinate: a controlled double-blind study in chronic
1052 schizophrenia. *Dis Nerv Syst* **36**, 361–364 (1975).
1053 29. Rome, B. N., Egilman, A. C., Patel, N. G. & Kesselheim, A. S. Using multiple authorized
1054 generics to maintain high prices: the example of entacapone. *Value in Health* **26**, 370–
1055 377 (2023).
1056 30. Ge, X. *et al.* SRS-FISH: A high-throughput platform linking microbiome metabolism to
1057 identity at the single-cell level. *Proc Natl Acad Sci USA* **119**, e2203519119 (2022).
1058 31. Vandeputte, D. *et al.* Quantitative microbiome profiling links gut community variation to
1059 microbial load. *Nature* **551**, 507–511 (2017).
1060 32. Altschul, S. F., Gish, W., Miller, W., Myers, E. W. & Lipman, D. J. Basic local alignment
1061 search tool. *J Mol Biol* **215**, 403–410 (1990).
1062 33. Kopf, S. H. *et al.* Trace incorporation of heavy water reveals slow and heterogeneous
1063 pathogen growth rates in cystic fibrosis sputum. *Proc Natl Acad Sci USA* **113**, E110–E116
1064 (2016).
1065 34. Berry, D. *et al.* Tracking heavy water (D2O) incorporation for identifying and sorting active
1066 microbial cells. *Proc Natl Acad Sci USA* **112**, E194–E203 (2015).
1067 35. Wegener, G., Kellermann, M. Y. & Elvert, M. Tracking activity and function of
1068 microorganisms by stable isotope probing of membrane lipids. *Curr Opin Biotechnol* **41**,
1069 43–52 (2016).
1070 36. Hong, W. *et al.* Antibiotic susceptibility determination within one cell cycle at single-
1071 bacterium level by stimulated Raman metabolic imaging. *Anal Chem* **90**, 3737–3743
1072 (2018).
1073 37. Zhang, L. *et al.* Spectral tracing of deuterium for imaging glucose metabolism. *Nat Biomed*
1074 *Eng* **3**, 402–413 (2019).
1075 38. Heuke, S. *et al.* Shot-noise limited tunable dual-vibrational frequency stimulated Raman
1076 scattering microscopy. *Biomed Opt Express* **12**, 7780 (2021).
1077 39. Zimmermann, M., Patil, K. R., Typas, A. & Maier, L. Towards a mechanistic understanding
1078 of reciprocal drug–microbiome interactions. *Mol Syst Biol* **17**, e10116 (2021).
1079 40. Orama, M., Tilus, P., Taskinen, J. & Lotta, T. Iron(III)-chelating properties of the novel
1080 catechol O-methyltransferase inhibitor entacapone in aqueous solution. *J Pharm Sci* **86**,
1081 827–831 (1997).

41. Tosato, M. & Di Marco, V. Metal chelation therapy and Parkinson's disease: a critical review on the thermodynamics of complex formation between relevant metal ions and promising or established drugs. *Biomolecules* **9**, 269 (2019).
42. Loomis, L. D. & Raymond, K. N. Solution equilibria of enterobactin and metal-enterobactin complexes. *Inorg Chem* **30**, 906–911 (1991).
43. Mayneris-Perxachs, J., Moreno-Navarrete, J. M. & Fernández-Real, J. M. The role of iron in host-microbiota crosstalk and its effects on systemic glucose metabolism. *Nat Rev Endocrinol* **18**, 683–698 (2022).
44. Lund, E. K., Wharf, S. G., Fairweather-Tait, S. J. & Johnson, I. T. Oral ferrous sulfate supplements increase the free radical-generating capacity of feces from healthy volunteers. *Am J Clin Nutr* **69**, 250–255 (1999).
45. Stintzi, A., Barnes, C., Xu, J. & Raymond, K. N. Microbial iron transport via a siderophore shuttle: A membrane ion transport paradigm. *Proc Natl Acad Sci USA* **97**, 10691–10696 (2000).
46. Rocha, E. R., de Uzeda, M. & Brock, J. H. Effect of ferric and ferrous iron chelators on growth of Bacteroides fragilis under anaerobic conditions. *FEMS Microbiol Lett* **84**, 45–50 (1991).
47. Ellermann, M. & Arthur, J. C. Siderophore-mediated iron acquisition and modulation of host-bacterial interactions. *Free Radic Biol Med* **105**, 68–78 (2017).
48. Chaumeil, P.-A., Mussig, A. J., Hugenholtz, P. & Parks, D. H. GTDB-Tk: a toolkit to classify genomes with the Genome Taxonomy Database. *Bioinformatics* **36**, 1925–1927 (2020).
49. Seyoum, Y., Baye, K. & Humblot, C. Iron homeostasis in host and gut bacteria – a complex interrelationship. *Gut Microbes* **13**, 1874855 (2021).
50. Ellermann, M. & Arthur, J. C. Siderophore-mediated iron acquisition and modulation of host-bacterial interactions. *Free Radic Biol Med* **105**, 68–78 (2017).
51. Feldgarden, M. *et al.* AMRFinderPlus and the Reference Gene Catalog facilitate examination of the genomic links among antimicrobial resistance, stress response, and virulence. *Sci Rep* **11**, 12728 (2021).
52. Lynch, J. B. & Hsiao, E. Y. Microbiomes as sources of emergent host phenotypes. *Science* **365**, 1405–1409 (2019).
53. Deleu, S., Machiels, K., Raes, J., Verbeke, K. & Vermeire, S. Short chain fatty acids and its producing organisms: An overlooked therapy for IBD? *eBioMedicine* **66**, (2021).
54. Dalile, B., Van Oudenhove, L., Vervliet, B. & Verbeke, K. The role of short-chain fatty acids in microbiota–gut–brain communication. *Nat Rev Gastroenterol Hepatol* **16**, 461–478 (2019).
55. Singh, A. N., Barlas, C., Saeedi, H. & Mishra, R. K. Effect of loxapine on peripheral dopamine-like and serotonin receptors in patients with schizophrenia. *J Psychiatry Neurosci* **28**, 39–47 (2003).
56. Weis, S. *et al.* Effect of Parkinson's disease and related medications on the composition of the fecal bacterial microbiota. *npj Parkinsons Dis.* **5**, 1–9 (2019).
57. Fu, S.-C. *et al.* A pilot study exploring the association ofentacapone, gut microbiota, and the subsequent side efects in patients with Parkinson's disease. *Front Cell Infect Microbiol* **12**, 837019 (2022).
58. Zhang, M. *et al.* Effects of metformin, acarbose, and sitagliptin monotherapy on gut microbiota in Zucker diabetic fatty rats. *BMJ Open Diab Res Care* **7**, e000717 (2019).
59. van Kessel, S. P. *et al.* Gut bacterial tyrosine decarboxylases restrict levels of levodopa in the treatment of Parkinson's disease. *Nat Commun* **10**, 310 (2019).
60. Dostal, A., Fehlbaum, S., Chassard, C., Zimmermann, M. B. & Lacroix, C. Low iron availability in continuous in vitro colonic fermentations induces strong dysbiosis of the child gut microbial consortium and a decrease in main metabolites. *FEMS Microbiol Ecol* **83**, 161–175 (2013).
61. Celis, A. I., Relman, D. A. & Huang, K. C. The impact of iron and heme availability on the healthy human gut microbiome in vivo and in vitro. *Cell Chem Biol* **30**, 110-126.e3 (2023).
62. Campbell, N. R. & Hasinoff, B. Ferrous sulfate reduces levodopa bioavailability: chelation as a possible mechanism. *Clin Pharmacol Ther* **45**, 220–225 (1989).

1137 63. Novartis Pharmaceuticals. Comtan® (entacapone) tablets: Prescribing information (US).
1138 New Jersey: Novartis Pharmaceuticals Corporation 2011.
1139 64. Vehreschild, M. J. G. T. *et al.* An open randomized multicentre Phase 2 trial to assess the
1140 safety of DAV132 and its efficacy to protect gut microbiota diversity in hospitalized patients
1141 treated with fluoroquinolones. *J Antimicrob Chemother* **77**, 1155–1165 (2022).
1142 65. Pjevac, P. *et al.* An Economical and Flexible Dual Barcoding, Two-Step PCR Approach
1143 for Highly Multiplexed Amplicon Sequencing. *Front Microbiol* **12**, 669776 (2021).
1144 66. Parada, A. E., Needham, D. M. & Fuhrman, J. A. Every base matters: assessing small
1145 subunit rRNA primers for marine microbiomes with mock communities, time series and
1146 global field samples. *Environ Microbiol* **18**, 1403–1414 (2016).
1147 67. Apprill A, McNally S, Parsons R, & Weber L. Minor revision to V4 region SSU rRNA 806R
1148 gene primer greatly increases detection of SAR11 bacterioplankton. *Aquat Microb Ecol*
1149 **75**, 129–137 (2015).
1150 68. Herbold, C. W. *et al.* A flexible and economical barcoding approach for highly multiplexed
1151 amplicon sequencing of diverse target genes. *Front Microbiol* **6**, 731 (2015).
1152 69. Callahan, B. J. *et al.* DADA2: High-resolution sample inference from Illumina amplicon
1153 data. *Nat Methods* **13**, 581–583 (2016).
1154 70. Callahan, B. J., Sankaran, K., Fukuyama, J. A., McMurdie, P. J. & Holmes, S. P.
1155 Bioconductor Workflow for Microbiome Data Analysis: from raw reads to community
1156 analyses. *F1000Res* **5**, 1492 (2016).
1157 71. Quast, C. *et al.* The SILVA ribosomal RNA gene database project: improved data
1158 processing and web-based tools. *Nucleic Acids Res* **41**, D590–D596 (2012).
1159 72. McMurdie, P. J. & Holmes, S. phyloseq: An R Package for Reproducible Interactive
1160 Analysis and Graphics of Microbiome Census Data. *PLoS One* **8**, e61217 (2013).
1161 73. Cole, J. R. *et al.* Ribosomal Database Project: data and tools for high throughput rRNA
1162 analysis. *Nucleic Acids Res* **42**, D633-642 (2014).
1163 74. Love, M. I., Huber, W. & Anders, S. Moderated estimation of fold change and dispersion
1164 for RNA-seq data with DESeq2. *Genome Biol* **15**, 550 (2014).
1165 75. Martin, M. Cutadapt removes adapter sequences from high-throughput sequencing reads.
1166 *EMBnet J* **17**, 10–12 (2011).
1167 76. Li, H. Minimap2: pairwise alignment for nucleotide sequences. *Bioinformatics* **34**, 3094–
1168 3100 (2018).
1169 77. Kolmogorov, M., Yuan, J., Lin, Y. & Pevzner, P. A. Assembly of long, error-prone reads
1170 using repeat graphs. *Nat Biotechnol* **37**, 540–546 (2019).
1171 78. Vaser, R., Sović, I., Nagarajan, N. & Šikić, M. Fast and accurate de novo genome
1172 assembly from long uncorrected reads. *Genome Res* **27**, 737–746 (2017).
1173 79. Li, H. *et al.* The Sequence Alignment/Map format and SAMtools. *Bioinformatics* **25**, 2078–
1174 2079 (2009).
1175 80. Kang, D. D. *et al.* MetaBAT 2: an adaptive binning algorithm for robust and efficient
1176 genome reconstruction from metagenome assemblies. *PeerJ* **7**, e7359 (2019).
1177 81. Gurevich, A., Saveliev, V., Vyahhi, N. & Tesler, G. QUAST: quality assessment tool for
1178 genome assemblies. *Bioinformatics* **29**, 1072–1075 (2013).
1179 82. Parks, D. H., Imelfort, M., Skennerton, C. T., Hugenholtz, P. & Tyson, G. W. CheckM:
1180 assessing the quality of microbial genomes recovered from isolates, single cells, and
1181 metagenomes. *Genome Res* **25**, 1043–55 (2015).
1182 83. Lowe, T. M. & Eddy, S. R. tRNAscan-SE: a program for improved detection of transfer
1183 RNA genes in genomic sequence. *Nucleic Acids Res* **25**, 955–964 (1997).
1184 84. Nawrocki, E. P. & Eddy, S. R. Infernal 1.1: 100-fold faster RNA homology searches.
1185 *Bioinformatics* **29**, 2933–2935 (2013).
1186 85. Ludwig, W. *et al.* ARB: a software environment for sequence data. *Nucleic Acids Res* **32**,
1187 1363–1371 (2004).
1188 86. Minh, B. Q. *et al.* IQ-TREE 2: new models and efficient methods for phylogenetic inference
1189 in the genomic era. *Mol Biol Evol* **37**, 1530–1534 (2020).
1190 87. Wagner, M., Horn, M. & Daims, H. Fluorescence in situ hybridisation for the identification
1191 and characterisation of prokaryotes. *Curr Opin Microbiol* **6**, 302–309 (2003).

88. Yilmaz, L. S., Parnerkar, S. & Noguera, D. R. mathFISH, a web tool that uses thermodynamics-based mathematical models for in silico evaluation of oligonucleotide probes for fluorescence in situ hybridization. *Appl Environ Microbiol* **77**, 1118–1122 (2011).
89. Manz, W., Amann, R., Ludwig, W., Wagner, M. & Schleifer, K.-H. Phylogenetic oligodeoxynucleotide probes for the major subclasses of Proteobacteria: problems and solutions. *Syst Appl Microbiol* **15**, 593–600 (1992).
90. Daims, H., Brühl, A., Amann, R., Schleifer, K. H. & Wagner, M. The domain-specific probe EUB338 is insufficient for the detection of all Bacteria: development and evaluation of a more comprehensive probe set. *Syst Appl Microbiol* **22**, 434–444 (1999).
91. Varel, V. H. & Bryant, M. P. Nutritional features of Bacteroides fragilis subsp. fragilis. *Appl Microbiol* **28**, 251–257 (1974).

Acknowledgements

Research reported in this manuscript was funded by NIH Awards R35GM136223 (to J.-X.C.) and R01AI141439 (to J.-X.C.) and supported by the Boston University Micro and Nano Imaging Facility and Office of the Director, NIH Award S10OD024993. The content is solely the responsibility of the authors and does not necessarily represent the official views of the NIH. Funding for the presented research was also provided via the Young Independent Research Group Grant ZK-57 (to F.C.P.) of the Austrian Science Fund (FWF) and the FWF-Wittgensteinaward Z383-B (to M.W.) as well as the FWF-funded Cluster of Excellence “Microbiomes drive Planetary Health” (COE 7). We thank Jasmin Schwarz, Gudrun Kohl, Petra Pjevac and Joana Seneca Silva from the Joint Microbiome Facility of the Medical University of Vienna and the University of Vienna for assisting with amplicon and metagenomic sequencing, as well as repositing of sequencing data.

Author contributions

F.C.P., X.G., J.-X.C. and M.W. designed this study. F.C.P, X.G., J.M.K., K.M. and M.D. performed the experiments with input from T.B, Y.Z., D.B. and A.S.. F.C.P, J.M.K., R.H.K, B.H., and K.W. analyzed sequencing data and performed bioinformatic analysis. F.C.P. and X.G. wrote the manuscript with input from all co-authors and all authors read and approved the final manuscript.

Ethics declarations

The authors declare no competing interests.